

# A Unitary Isobar Model for Pion Photo- and Electroproduction on the Proton up to 1 GeV

D. Drechsel, O. Hanstein, S. S. Kamalov\* and L. Tiator

*Institut für Kernphysik, Universität Mainz, 55099 Mainz, Germany*

(February 9, 2008)

A new operator for pion photo- and electroproduction has been developed for nuclear applications at photon equivalent energies up to 1 GeV. The model contains Born terms, vector mesons and nucleon resonances ( $P_{33}(1232)$ ,  $P_{11}(1440)$ ,  $D_{13}(1520)$ ,  $S_{11}(1535)$ ,  $F_{15}(1680)$ , and  $D_{33}(1700)$ ). The resonance contributions are included taking into account unitarity to provide the correct phases of the pion photoproduction multipoles. The  $Q^2$  dependence of electromagnetic resonance vertices is described with appropriate form factors in the electromagnetic helicity amplitudes. Within this model we have obtained good agreement with the experimental data for pion photo- and electroproduction on the nucleon for both differential cross sections and polarization observables. The model can be used as a starting point to predict and analyze forthcoming data.

## I. INTRODUCTION

Pion photo- and electroproduction is presently one of the main sources of our information on the structure of nucleons and nuclei. With the advent of the new generation of high intensity, high duty-factor electron accelerators as Jefferson Lab (Newport News), MAMI (Mainz) and ELSA (Bonn), as well as modern laser backscattering facilities as LEGS (Brookhaven) and GRAAL (Grenoble), this field reaches a new level of promise.

The elementary amplitude of pion photo- and electroproduction on free nucleons is one of the main ingredients of the analysis of these reactions for nuclei. It has been the subject of extensive theoretical and experimental studies, and over the past 30 years a series of models was developed for photon energies from threshold up to 500 MeV (see for example Refs. [1-5] and references therein). Attempts to extend these models to energies up to around 1 GeV, by use of effective Lagrangians and coupled channels approaches, have been presented in Refs. [6,7] and [8]. Unfortunately, most of the recent models are too sophisticated and complicated and difficult to handle for nuclear applications.

A simple and effective model for nuclear calculations was developed in the late 70's by Blomqvist and Laget [9]. It provided an adequate description of then available experimental data up to the first resonance region. However, in the mean time modern electron accelerators have provided a host of new high precision data. Beams of high current and high duty-factor have reduced the statistical errors to the order of a few percent, and the new data have provided us with high quality multipole analyses of pion photoproduction from VPI [10] and Mainz [11].

With such advances it is certainly appropriate to develop new models for the description of pion photo- and electroproduction. With respect to nuclear applications, these models should have a simple and physically transparent form. On the other hand they should satisfy gauge invariance and unitarity, and reproduce the existing experimental data, not only in the first but also in the second and third resonance regions, for both pion photo- and electroproduction, which are the subject of the current interest. It is therefore the aim of this work to develop a model having these properties.

As a starting point we will use the prescriptions of the isobar model [12,13], assuming that resonance contributions in the relevant multipoles have Breit-Wigner forms. The  $Q^2$  dependence of the  $\gamma NN^*$  vertices will be determined via the corresponding helicity amplitudes or quark multipole moments [14]. The nonresonant contributions will be described using standard Born terms with a mixed pseudovector-pseudoscalar  $\pi NN$  coupling and vector meson exchange. The final amplitude will be unitarized by extending the procedure developed by Olsson [15] and Laget [16] to the case of virtual photons and higher resonances. Finally we demonstrate that such an extremely economical model provides a good description for individual multipoles as well as differential cross sections and polarization observables. We believe that the developed model can be used not only for nuclear applications, but also as a starting point to predict and analyze forthcoming data for pion photo- and electroproduction on proton and neutron targets.

---

\*Permanent address: Laboratory of Theoretical Physics, JINR Dubna, Head Post Office Box 79, SU-101000 Moscow, Russia.

## II. FORMALISM

In the following we will briefly summarize the most important expressions which clarify the conventions used in our paper. For details we refer to, e.g. Ref. [1].

In accordance with Ref. [1] we decompose the current operator in the  $\pi N$  *cm* frame into the standard CGLN amplitudes  $F_i$  [18,19]

$$\begin{aligned} \mathbf{J} &= \frac{4\pi W}{m_N} \left[ i\tilde{\sigma}F_1 + (\boldsymbol{\sigma} \cdot \hat{\mathbf{q}})(\boldsymbol{\sigma} \times \hat{\mathbf{k}})F_2 + i\tilde{\mathbf{q}}(\boldsymbol{\sigma} \cdot \hat{\mathbf{k}})F_3 \right. \\ &\quad \left. + i\tilde{\mathbf{q}}(\boldsymbol{\sigma} \cdot \hat{\mathbf{q}})F_4 + i\hat{\mathbf{k}}(\boldsymbol{\sigma} \cdot \hat{\mathbf{k}})F_5 + i\hat{\mathbf{k}}(\boldsymbol{\sigma} \cdot \hat{\mathbf{q}})F_6 \right], \\ \rho &= \frac{4\pi W}{m_N} \left[ i(\boldsymbol{\sigma} \cdot \hat{\mathbf{q}})F_7 + i(\boldsymbol{\sigma} \cdot \hat{\mathbf{k}})F_8 \right] = \frac{\mathbf{k} \cdot \mathbf{J}}{\omega}, \end{aligned} \quad (1)$$

where  $m_N$  and  $\boldsymbol{\sigma}$  are the mass and spin operator of the nucleon respectively,  $W$  is the total energy of the  $\pi N$  system,  $\hat{\mathbf{k}} = \mathbf{k} / |\mathbf{k}|$  and  $\hat{\mathbf{q}} = \mathbf{q} / |\mathbf{q}|$  are the unit vectors for the photon and pion momenta respectively, and  $\tilde{\mathbf{a}} = \mathbf{a} - (\mathbf{a} \cdot \hat{\mathbf{k}})\hat{\mathbf{k}}$  represents a vector with purely transverse components. The eight amplitudes  $F_1, \dots, F_8$  are complex functions of three independent variables, e.g. the total energy  $W$ , the pion angle  $\theta_\pi$ , and the four-momentum squared of the virtual photon,  $Q^2 = \mathbf{k}^2 - \omega^2 > 0$ . Due to current conservation we obtain the two relations  $|\mathbf{k}|F_5 = \omega F_8$  and  $|\mathbf{k}|F_6 = \omega F_7$ . Therefore only six amplitudes are independent. In the present work we use  $F_1, \dots, F_6$ .

For the analysis of the experimental data and also in order to study individual baryon resonances, pion photo- and electroproduction amplitudes are usually expressed in terms of three types of multipoles, electric ( $E_{l\pm}$ ), magnetic ( $M_{l\pm}$ ), and longitudinal ( $L_{l\pm}$ ) ones, with pion angular momentum  $l$  and total angular momentum  $j = l \pm 1/2$ . They are defined by a multipole decomposition of the amplitudes  $F_i$ ,

$$\begin{aligned} F_1 &= \sum_{l \geq 0} \{(lM_{l+} + E_{l+})P'_{l+1} + [(l+1)M_{l-} + E_{l-}]P'_{l-1}\}, \\ F_2 &= \sum_{l \geq 1} [(l+1)M_{l+} + lM_{l-}]P'_l, \\ F_3 &= \sum_{l \geq 1} [(E_{l+} - M_{l+})P''_{l+1} + ((E_{l-} + M_{l-})P''_{l-1})], \\ F_4 &= \sum_{l \geq 2} (M_{l+} - E_{l+} - M_{l-} - E_{l-})P''_l, \\ F_5 &= \sum_{l \geq 0} [(l+1)L_{1+}P'_{l+1} - lL_{l-}P'_{l-1}], \\ F_6 &= \sum_{l \geq 1} [lL_{1-} - (l+1)L_{l+}]P'_l, \end{aligned} \quad (2)$$

where  $P'_l$  are the derivatives of the Legendre polynomials. Note that in the literature the longitudinal transitions are often described by  $S_{l\pm}$  multipoles, which correspond to the multipole decomposition of the amplitudes  $F_7$  and  $F_8$ . They are connected with the longitudinal ones by  $S_{l\pm} = |\mathbf{k}| L_{l\pm} / \omega$ .

From total isospin conservation in the pion-nucleon system it follows that the amplitudes  $F_i$  (or the multipoles) can be expressed in terms of three independent isospin amplitudes [19]. These are  $A^{(0)}$  for the isoscalar photon, and for the isovector photon the two amplitudes  $A^{(1/2)}$  and  $A^{(3/2)}$  for the  $\pi N$  system with total isospin  $I = 1/2$  and  $I = 3/2$  respectively. However, it is also useful to define the proton  ${}_p A^{(1/2)}$  and neutron  ${}_n A^{(1/2)}$  amplitudes with total isospin  $1/2$ ,

$${}_p A^{(1/2)} = A^{(0)} + \frac{1}{3}A^{(1/2)}, \quad {}_n A^{(1/2)} = A^{(0)} - \frac{1}{3}A^{(1/2)}. \quad (3)$$

With this convention the physical amplitudes for the four physical pion photo- and electroproduction processes are

$$\begin{aligned} A(\gamma^* p \rightarrow n\pi^+) &= \sqrt{2} \left[ {}_p A^{(1/2)} - \frac{1}{3}A^{(3/2)} \right], & A(\gamma^* p \rightarrow p\pi^0) &= {}_p A^{(1/2)} + \frac{2}{3}A^{(3/2)}, \\ A(\gamma^* n \rightarrow p\pi^-) &= \sqrt{2} \left[ {}_n A^{(1/2)} + \frac{1}{3}A^{(3/2)} \right], & A(\gamma^* n \rightarrow n\pi^0) &= - {}_n A^{(1/2)} + \frac{2}{3}A^{(3/2)}. \end{aligned} \quad (4)$$

All the observables for these processes may be expressed in terms of the amplitudes  $F_i$ . In general there are 16 different polarization observables for the reactions with real photons. In pion electroproduction we have four additional observables due to the longitudinal amplitudes  $F_5$  and  $F_6$  and 16 observables due to longitudinal-transverse interference, giving a total number of 36 polarization observables. In the literature there occur many different definitions for these observables. In our work we shall mainly follow the convention of Ref. [17]. In the case of comparison with experimental data presented in different conventions, we will give special comments.

### III. BACKGROUND

#### A. Born and vector mesons exchange terms

As pointed out in the introduction, the main goal of our present work is to develop a simple model for nuclear applications, which should be consistent with the recent data for pion photo- and electroproduction on nucleons at photon energies (or equivalent energies) up to 1 GeV. This energy range covers the first and second, and touches the third resonance regions. The base line for a correct description of the resonance contributions is, of course, a reliable description of the nonresonant part of the amplitude (nonresonant background). Traditionally this part is described by evaluation of the Feynman diagrams derived from an effective Lagrangian density. For the electromagnetic  $\gamma NN$  and  $\gamma\pi\pi$  vertices the structure is well defined,

$$\mathcal{L}_{\gamma NN} = -e\bar{\psi} \left[ \gamma_\mu \mathcal{A}^\mu F_1^{p,n}(Q^2) + \frac{\sigma_{\mu\nu}}{2m_N} \partial^\mu \mathcal{A}^\nu F_2^{p,n}(Q^2) \right] \psi, \quad (5)$$

$$\mathcal{L}_{\gamma\pi\pi} = e [(\partial_\mu \boldsymbol{\pi})^\dagger \times \boldsymbol{\pi}]_3 \mathcal{A}^\mu F_\pi(Q^2), \quad (6)$$

where  $\mathcal{A}^\mu$  is the electromagnetic vector potential,  $\psi$  and  $\boldsymbol{\pi}$  are the nucleon and pion field operators, respectively. In Eqs. (5-6) we have included explicitly  $Q^2$  dependent proton ( $F_{1,2}^p$ ), neutron ( $F_{1,2}^n$ ) and pion ( $F_\pi$ ) electromagnetic form factors. In the case of real photons the form factors are normalized to  $F_1^p(0) = F_\pi(0) = 1$ ,  $F_1^n(0) = 0$ ,  $F_2^p(0) = \kappa_p = 1.79$  and  $F_2^n(0) = \kappa_n = -1.97$ . For virtual photons we express the nucleon form factors in terms of the Sachs form factors by the standard dipole form, and assume that  $F_\pi(Q^2) = F_1^p(Q^2) - F_1^n(Q^2)$  which is the simplest way to preserve gauge invariance. In the same way we treat the axial form factor  $F_A(Q^2)$ .

The description of the hadronic  $\pi NN$  system is a more sophisticated part of the theory of pion photo- and electroproduction. In this case there are two possibilities for the construction of the interaction Lagrangian, the pseudoscalar (PS),

$$\mathcal{L}_{\pi NN}^{\text{PS}} = ig\bar{\psi}\gamma_5\boldsymbol{\tau}\cdot\psi\boldsymbol{\pi}, \quad (7)$$

and the pseudovector (PV),

$$\mathcal{L}_{\pi NN}^{\text{PV}} = -\frac{f}{m_\pi}\bar{\psi}\gamma_5\gamma_\mu\boldsymbol{\tau}\cdot\partial^\mu\boldsymbol{\pi}\psi, \quad (8)$$

$\pi NN$  coupling, where  $g^2/4\pi = 14.28$  and  $f/m_\pi = g/2m_N$ . At low pion energies the PV coupling is to be preferred, because it fulfills PCAC and is consistent with low energy theorems (LET) and chiral perturbation theory to leading order. However, the PV model cannot be renormalized in the usual way, and this produces a problem at high energies. On the other hand, the renormalizable PS model leads to a better description at the higher photon energies. In our work we consider both of these schemes by a gradual transition between them.

The final expressions for the CGLN amplitudes  $F_1, \dots, F_6$ , obtained using the effective Lagrangians (5-8) are well-known (see, for example Ref. [19]). We will refer to them as *Born term contributions*. They are the dominant part of our background. The other part is related to *vector meson exchange contributions*. In general they are much smaller, but as we will show below they are quite important for some multipoles. The effective Lagrangians for  $\omega$  and  $\rho$  exchange are [4]

$$\mathcal{L}_{\gamma\pi V} = e\frac{\lambda_V}{m_\pi} \epsilon_{\mu\nu\rho\sigma} (\partial^\mu A^\nu) \pi_i \partial^\rho (\delta_{i3}\omega^\sigma + \rho_i^\sigma) F_V(Q^2), \quad (9)$$

$$\mathcal{L}_{VNN} = \bar{\psi} \left( g_{V1}\gamma_\mu + \frac{g_{V2}}{2m_N} \sigma_{\mu\nu} \partial^\nu \right) (\omega^\mu + \boldsymbol{\tau}\cdot\boldsymbol{\rho}^\mu) \psi, \quad (10)$$

where  $\omega$  and  $\rho$  are the  $\omega$  and  $\rho$  meson field operators respectively, and  $\lambda_V$  is the radiative coupling determined by  $V \rightarrow \pi\gamma$  decay. The  $Q^2$  dependence of  $\mathcal{L}_{\gamma\pi V}$  is defined using a dipole form factor.

In general the values for the strong coupling constants  $g_{V1}$  (vector coupling) and  $g_{V2}$  (tensor coupling) in Eq. (10), are not well determined. In various analyses they vary in the ranges [3,20] of  $8 \leq g_{\omega 1} \leq 20$ ,  $1.8 \leq g_{\rho 1} \leq 3.2$ ,  $-1 \leq g_{\omega 2}/g_{\omega 1} \leq 0$  and  $4.3 \leq g_{\rho 2}/g_{\rho 1} \leq 6.6$ . In the present work we take them as free parameters to be varied within these ranges. The off-shell behaviour of the vertex functions is described by hadronic monopole form factors,

$$g_{Vi} = \frac{\Lambda_V^2}{\Lambda_V^2 + \mathbf{k}_V^2} \tilde{g}_{Vi}. \quad (11)$$

## B. Nonresonant multipoles

From the considerations above we find that the following ingredients for the construction of the background are not well defined: 1) the type of the  $\pi NN$  coupling and 2) the coupling constants for the vector meson exchange contributions. The best way to fix them is to analyse nonresonant  $s$ - and  $p$ -wave multipoles. In our energy region these are  $E_{0+}^{(3/2)}$ ,  $M_{1-}^{(3/2)}$ ,  ${}_{p,n}M_{1+}^{(1/2)}$ , and  ${}_{p,n}E_{1+}^{(1/2)}$ . At photon *lab* energies  $E_\gamma < 500$  MeV, the multipole  ${}_{p,n}E_{0+}^{(1/2)}$  can also be considered as nonresonant.

First, let us fix the coupling constants of the vector mesons. For this purpose we consider the multipoles which are independent of the type of the  $\pi NN$  coupling. These are  ${}_{p,n}M_{1+}^{(1/2)}$  and  ${}_{p,n}E_{1+}^{(1/2)}$ , of which the first one ( $M_{1+}$ ) is especially sensitive to  $\omega$  exchange contributions, as illustrated in Fig. 1. The final results for the coupling constants and cut-off parameters  $\Lambda_V$  are given in Table 1.

The real parts of the nonresonant multipoles  $E_{0+}$  and  $M_{1-}$  in the isospin 3/2 channel are more appropriate to fix the optimum parametrization for the  $\pi NN$  coupling. In Fig. 2 we have depicted their energy dependence obtained with PS (dotted curves) and PV (dashed curves) couplings. In the threshold region the best description of recent analyses from VPI [10] and Mainz [11] can be obtained within a PV model. As pointed out before, this coupling has also to be preferred on general grounds, because it reproduces the leading terms of ChPT near threshold. However, at larger photon energies ( $E_\gamma > 600$  MeV) the results of the VPI group are in between our calculations with PV and PS couplings. In such a situation, in order to describe  $E_{0+}^{(3/2)}$  and  $M_{1-}^{(3/2)}$  multipole in a wide energy range up to  $E_\gamma = 1$  GeV, the most economical way is to construct a *hybrid model* (HM) with a mixed type of  $\pi NN$  coupling. In order to give a reasonable threshold behavior, it has to start with pure pseudovector coupling at the lowest energy and will develop into pseudoscalar coupling at the highest energies. The simplest effective Lagrangian for such a model may be written in the form

$$\mathcal{L}_{\pi NN}^{HM} = \frac{\Lambda_m^2}{\Lambda_m^2 + \mathbf{q}_0^2} \mathcal{L}_{\pi NN}^{PV} + \frac{\mathbf{q}_0^2}{\Lambda_m^2 + \mathbf{q}_0^2} \mathcal{L}_{\pi NN}^{PS}, \quad (12)$$

where  $\mathbf{q}_0$  is the asymptotic pion momentum in the  $\pi N$  *cm* frame which depends only on  $W$  and is not an operator acting on the pion field. From the analysis of the  $M_{1-}^{(3/2)}$  and  $E_{0+}^{(3/2)}$  multipoles we have found that the most appropriate value for the mixing parameter is  $\Lambda_m = 450$  MeV. We note that for the pion pole terms the pion couples with on-shell nucleons only, and HM, PV and PS models are all equivalent. Moreover, only the multipoles  $E_{0+}$ ,  $M_{1-}$ ,  $L_{0+}$ , and  $L_{1-}$  are affected by changing the coupling schemes.

One of the important peculiarities of the  $E_{0+}$  multipoles is the relatively large imaginary part, even at low pion energies. The origin of this feature is well-known: pion-nucleon rescattering (or final  $\pi N$  interaction). In order to take account of this effect, we shall use a prescription in accordance with unitarity (Fermi-Watson theorem) and K-matrix approach, i.e.

$$E_{0+}^{(I)} = E_{0+}^{(I)}(\text{Born} + \omega, \rho) (1 + i t_{\pi N}^I), \quad (13)$$

where  $t_{\pi N}^I = [\eta_I \exp(i\delta_{\pi N}^I) - 1]/2i$  is the pion-nucleon elastic scattering amplitude with the phase shift  $\delta_{\pi N}^I$  and the inelasticity parameter  $\eta_I$  (both taken from the VPI analysis).

In Fig. 2 (solid curve) we see that the unitarity condition (13) combined with our Lagrangian (12) provides an excellent description of the real and imaginary parts of the  $E_{0+}^{(3/2)}$  multipole in a wide energy range. In Fig. 2 we illustrate similar results for the case of isospin 1/2 and  $E_\gamma < 550$  MeV. In the next section we will describe the analysis of the latter channel for the higher energies in connection with  $S_{11}(1535)$  resonance excitation.

Finally we note that in the charged pion channels the multipole  $E_{0+}$  is not sensitive to different choices of the  $\pi NN$  coupling and contributions of pion rescattering. However, these effects are extremely important in the neutral channels for both the  $E_{0+}$  and  $L_{0+}$  multipoles. In the latter case we predict a large imaginary part that certainly has to be taken into account in future analyses of the  $(e, e' \pi^0)$  reaction, e.g., in the transverse-longitudinal (TL) cross section, where the nonresonant  $\text{Im}\{L_{0+}\}$  multipole interferes with the large resonant  $\text{Im}\{M_{1+}\}$  multipole.

#### IV. RESONANCE CONTRIBUTIONS - REAL PHOTONS

The background contributions being fixed, we can develop a reliable scheme to study baryon resonances by analyzing the relevant multipoles. However, it is well-known (see e.g. Ref. [11]), that even in this case the procedure for the extraction of the "bare" resonance contributions is not trivial due to the interference with the background. In the present work we generally consider so-called "dressed" resonances which include "bare" resonances and vertex corrections due to the interference with the background. We believe that for nuclear applications this is a more appropriate way to facilitate the investigation of medium effects. On the other hand, the K-matrix approach asserts that at resonance position the contribution from the interference term is small or even vanishing in the case of an ideal resonance. Therefore, we expect to get reliable informations about the conventional resonance parameters at the position of the resonance.

First we consider pion photoproduction. For the relevant multipoles  $A_{l\pm}$  we describe the resonance contributions assuming a Breit-Wigner energy dependence of the form

$$A_{l\pm}(W) = \bar{A}_{l\pm} f_{\pi N}(W) \frac{\Gamma_{tot} W_R e^{i\phi}}{W_R^2 - W^2 - iW_R \Gamma_{tot}} f_{\pi N}(W) C_{\pi N}, \quad (14)$$

where  $f_{\pi N}(W)$  is the usual Breit-Wigner factor describing the decay of the  $N^*$  resonance with total width  $\Gamma_{tot}$ , partial  $\pi N$ -width  $\Gamma_{\pi N}$  and spin  $j$ ,

$$f_{\pi N}(W) = \left[ \frac{1}{(2j+1)\pi} \frac{k_W}{|\mathbf{q}|} \frac{m_N}{W} \frac{\Gamma_{\pi N}}{\Gamma_{tot}^2} \right]^{1/2}, \quad k_W = \frac{W^2 - m_N^2}{2W}. \quad (15)$$

The factor  $C_{\pi N}$  is  $\sqrt{3/2}$  and  $-1/\sqrt{3}$  for the isospin  $3/2$  and isospin  $1/2$  multipoles respectively, as defined by Eq. (3).

In accordance with Refs. [9,12] the energy dependence of the partial width  $\Gamma_{\pi N}$  is given by

$$\Gamma_{\pi N} = \beta_\pi \Gamma_R \left( \frac{|\mathbf{q}|}{q_R} \right)^{2l+1} \left( \frac{X^2 + q_R^2}{X^2 + \mathbf{q}^2} \right)^l \frac{W_R}{W}, \quad (16)$$

where  $X$  is a damping parameter, assumed to be  $X = 500$  MeV for all resonances.  $\Gamma_R$  and  $q_R$  are the total width and the pion *cm* momentum at the resonance peak ( $W = W_R$ ) respectively, and  $\beta_\pi$  is the single-pion branching ratio.

The total width  $\Gamma_{tot}$  in Eqs.(14-15) is the sum of  $\Gamma_{\pi N}$  and the "inelastic" width  $\Gamma_{in}$ . For the latter one we assume dominance of the two-pion decay channels and parametrize the corresponding energy dependence as in Ref. [21],

$$\Gamma_{tot} = \Gamma_{\pi N} + \Gamma_{in}, \quad \Gamma_{in} = (1 - \beta_\pi) \Gamma_R \left( \frac{q_{2\pi}}{q_0} \right)^{2l+4} \left( \frac{X^2 + q_0^2}{X^2 + q_{2\pi}^2} \right)^{l+2}, \quad (17)$$

where  $q_{2\pi}$  is the momentum of the compound  $(2\pi)$  system with mass  $2m_\pi$  and  $q_0 = q_{2\pi}$  at  $W = W_R$ . Concerning the definition of  $\Gamma_{in}$ , it takes into account the correct energy behavior of the phase space near the three-body threshold. We make an exception for the  $S_{11}(1535)$  resonance, where we also introduce a  $\eta N$  width, similar to Eq. (16) but with the mass  $m_\eta = 547$  MeV.

The main parameters in the  $\gamma NN^*$  vertex are the electromagnetic amplitudes  $\bar{A}_{l\pm}$ , introduced in Ref. [22]. They are linear combinations of the usual electromagnetic helicity amplitudes  $A_{1/2}$  and  $A_{3/2}$  (see, e.g., Eq. (1) in Ref. [22]). We parametrize the  $W$  dependence of the  $\gamma NN^*$  vertex beyond the resonance peak with a form factor

$$f_{\gamma N}(W) = \left( \frac{k_W}{k_R} \right)^n \left( \frac{X^2 + k_R^2}{X^2 + k_W^2} \right), \quad n \geq l_\gamma, \quad (18)$$

where the damping parameter  $X$  is the same as in Eqs.(16-17) and  $k_R = k_W$  at  $W = W_R$ . In order to preserve the correct "pseudothreshold" behaviour, mainly given by the Born terms, we introduce a parameter  $n \geq l_\gamma$ , with  $l_\gamma$  the orbital angular momentum of the photon.

One important ingredient of the Breit-Wigner parametrization (14) is the unitary phase  $\phi$ . The main role of this parameter is to adjust the phase  $\psi$  of the total multipole (background plus resonance) to the corresponding pion-nucleon scattering phase  $\delta_{\pi N}$  (in accordance with the Fermi-Watson theorem, when the influence of the inelastic channels is small) or to the experimentally observed phase. The latter procedure will become necessary when the photon energy increases above 500 MeV, the approximate limit of the Fermi-Watson theorem.

For the most important  $\Delta(1232)$  resonance ( $M_{1+}^{(3/2)}$  and  $E_{1+}^{(3/2)}$  multipoles), the influence of the inelastic channels is negligibly small up to  $E_\gamma \approx 800$  MeV. In this region  $\psi = \delta_{\pi N}$  with very good accuracy. At the higher energies, where the  $\Delta$  contribution becomes small, we will use the ansatz [23]

$$\psi_l^I(W) = \arctan \left[ \frac{1 - \eta_l^I(W) \cos 2\delta_l^I(W)}{\eta_l^I(W) \sin 2\delta_l^I(W)} \right]. \quad (19)$$

The pion-nucleon scattering phases  $\delta_l^I$  and inelasticity parameters  $\eta_l^I$  are taken from the analysis of the VPI group (SAID program). Then, applying the unitarization procedure developed by Olsson [15] and Laget [16], we can determine the phase  $\phi(W)$ . The results of our fit to the  $M_{1+}^{(3/2)}$  and  $E_{1+}^{(3/2)}$  multipoles are shown on Fig. 3, and the corresponding phases  $\phi(W)$  are given in the appendix.

We apply the same procedure to the  $P_{11}(1440)$  resonance and the corresponding multipoles  ${}_p M_{1-}^{(1/2)}$  and  ${}_n M_{1-}^{(1/2)}$ . However, in this case the influences of the inelastic channels on the pion photoproduction phase become important already at  $E_\gamma > 450$  MeV, and they are different in the proton and neutron channels. In this situation we define  $\phi(W)$  by using the results of the VPI analysis.

In the second and third resonance regions the most important resonances are the  $S_{11}(1535)$  contributing to the  $E_{0+}^{(1/2)}$  multipole, the  $D_{13}(1520)$  with contributions to the  $E_{2-}^{(1/2)}$  and  $M_{2-}^{(1/2)}$  multipoles, and the  $F_{15}(1680)$  with contributions to the  $E_{3-}^{(1/2)}$  and  $M_{3-}^{(1/2)}$  multipoles. In the isospin 3/2 channel the most important resonance is the  $D_{33}(1700)$  which contributes to the  $E_{2-}^{(3/2)}$  and  $M_{2-}^{(3/2)}$  multipoles. Unfortunately, for all these multipoles little information is available about the phases beyond the resonance peak. Therefore, in these cases we consider  $\phi$  a free parameter that we take as a constant extracted from the observed ratio between the imaginary and real parts at the resonance peak.

The final results for the more important multipoles and the corresponding values for the resonance parameters are presented in Figs. 4-6 and Tables 2-3, respectively. We note that the  $\gamma NN^*$  vertex at resonance is described by the two helicity amplitudes  $A_{1/2}$  and  $A_{3/2}$ . These can be easily extracted from the imaginary part of Eq. (14) using the values for the electromagnetic amplitudes  $\bar{A}_{l\pm}$ , the phases  $\phi_R = \phi(W = W_R)$ , and Eq. (1) of Ref. [22]. For example, we find in the case of the  $\Delta$  resonance

$$\begin{aligned} A_{1/2} &= -(3\bar{\mathcal{E}}_{1+}^{(3/2)} \cos \phi_E + \bar{\mathcal{M}}_{1+}^{(3/2)} \cos \phi_M)/2, \\ A_{3/2} &= \sqrt{3}(\bar{\mathcal{E}}_{1+}^{(3/2)} \cos \phi_E - \bar{\mathcal{M}}_{1+}^{(3/2)} \cos \phi_M)/2. \end{aligned} \quad (20)$$

Our values for the helicity amplitudes are summarized in Table 4. In general they are in the range of the recent Particle Data Group (PDG) analysis [24], the only exception being the case of the neutron  $P_{11}$  amplitude.

In Figs. 7-8 we compare our results (solid curves) for differential cross sections, photon ( $\Sigma$ ) and target ( $T$ ) asymmetries with the recent dispersion relation analysis of Mainz [11] (dashed curves), and with old and new data from Bonn and Mainz in the first resonance region. One can see that our model describes the observables in this region at the same level of accuracy as dispersion relations. Moreover, in this energy region our model can be extremely simplified by keeping only contributions from  $P_{33}(1232)$  and  $P_{11}(1440)$  resonances, and the calculations with pure PV  $\pi NN$  coupling and with our hybrid model differ very little.

In Figs. 9-12 we present our results (solid curves) for the differential cross sections and single polarization observables at  $E_\gamma > 450$  MeV, where the contributions from the second and third resonance regions become increasingly important. Our complete model generally agrees well with the experimental data in the  $\pi^+ n$  channel over a wide energy region up to 1 GeV. However, there is one exception, the differential cross section at 700 MeV. From Fig. 4 we can see that this is the region where the  $S_{11}(1535)$  resonance has a maximum contribution due to a cusp effect. In this region calculations without the  $S_{11}$  resonance (dashed curves) describe the data better. In the  $\pi^0 p$  channel we could only obtain a satisfactory agreement with the data up to  $E_\gamma < 900$  MeV. Unfortunately, the data sets of different groups are not consistent in that channel, and the error bars are much bigger than in the case of the data at lower energies.

In Fig. 13 we demonstrate the evolution of the energy distribution in the  $\pi^+ n$  channel at backward angles by subsequent addition of resonance contributions to the Born terms. First, we see that the large contribution from (non unitarized!) Born terms is strongly suppressed by the  $\Delta$  resonance. The second interesting feature is related to the excitations of the  $S_{11}(1535)$  and  $D_{13}(1520)$  resonances. At  $\theta_\pi = 120^\circ$  their contributions are comparable and it is difficult to separate them. However, at  $\theta_\pi = 180^\circ$  the contribution of the  $D_{13}(1520)$  resonance is very small, because the  $E_{2-}$  multipole vanishes at this kinematics. This fact provides a possibility to study the contribution from the  $S_{11}(1535)$  resonance and the related cusp effect due to the opening of the  $\eta$  channel, clearly separated from  $D_{13}(1520)$  effects.

## V. RESONANCE CONTRIBUTIONS - VIRTUAL PHOTONS

The major problem in the extension of our model to the case of virtual photons is associated with the determination of the  $Q^2$  dependence of the amplitudes  $\bar{A}_{l\pm}(Q^2)$  at the resonance peak. For the main  $\bar{\mathcal{M}}_{1+}^{(3/2)}$  amplitude we define this dependence by

$$\bar{\mathcal{M}}_{1+}^{(3/2)}(Q^2) = \bar{\mathcal{M}}_{1+}^{(3/2)}(0) \frac{|\mathbf{k}|}{k_W} e^{-\gamma Q^2} F_D(Q^2), \quad (21)$$

where  $F_D$  is the usual dipole form factor. The parameter  $\gamma$  will be determined later. Note that in Eq. (21) an additional  $Q^2$  dependence appears due to the kinematical factor  $|\mathbf{k}|/k_W$ , with the virtual photon three-momentum

$$\mathbf{k}^2 = Q^2 + \frac{(W^2 - m_N^2 - Q^2)^2}{4W^2} = Q^2 + \omega^2. \quad (22)$$

At present time there is only little experimental information available on the  $Q^2$  dependence of the small  $E_{1+}^{(3/2)}$  and  $S_{1+}^{(3/2)}$  multipoles. Following Ref. [16], we therefore assume that the corresponding electromagnetic amplitudes have the same  $Q^2$  dependence as  $\bar{\mathcal{M}}_{1+}^{(3/2)}$ ,

$$\begin{aligned} \bar{\mathcal{E}}_{1+}^{(3/2)}(Q^2) &= \bar{\mathcal{E}}_{1+}^{(3/2)}(0) \frac{|\mathbf{k}|}{k_W} e^{-\gamma Q^2} F_D(Q^2), \\ \bar{\mathcal{S}}_{1+}^{(3/2)}(Q^2) &= \bar{\mathcal{E}}_{1+}^{(3/2)}(Q^2) = \frac{|\mathbf{k}|}{\omega} \bar{\mathcal{L}}_{1+}^{(3/2)}(Q^2). \end{aligned} \quad (23)$$

Of course, this assumption will have to be checked whenever more information about the  $E_{1+}/M_{1+}$  and  $S_{1+}/M_{1+}$  ratios will be available from the new experiments.

The extension of the unitarization procedure to the case of pion electroproduction is straightforward for the  $\Delta$ -resonance, because the Fermi-Watson theorem requires that the phases of the total  $M_{1+}^{(3/2)}$ ,  $E_{1+}^{(3/2)}$  and  $S_{1+}^{(3/2)}$  multipoles should not depend on  $Q^2$ . Therefore, the position of the resonance peak does not depend on  $Q^2$  either. In our model this important requirement is satisfied by an appropriate choice of the phase  $\phi$  in Eq. (14). We note that after the unitarization procedure this phase will depend not only on  $W$  but also on  $Q^2$ . In this way we always obtain resonance multipoles with real parts vanishing at the resonance position  $W = 1232$  MeV and with the total phases of the multipoles equal to  $90^\circ$ . In Fig. 14 we give our predictions for the  $M_{1+}^{(3/2)}$  and  $E_{1+}^{(3/2)}$  multipoles at  $Q^2=0, 0.2$ , and  $1.0$  (GeV/c) $^2$  which satisfy this requirement. Note that the  $E_{1+}^{(3/2)}$  multipole has a second zero immediately above the resonance peak. Its position is  $Q^2$  dependent, and in accordance with unitarity the real and imaginary parts simultaneously change sign. The obtained unitary phases  $\phi$  as a function of  $Q^2$  and  $W$  are given in the appendix.

In Fig. 15 we show our unitarized  $M_{1+}^{(3/2)}$  multipole as a function of  $Q^2$  at  $W = 1232$  MeV. The experimental data were extracted from the magnetic  $G_M^*$  form factor using the relation

$$M_{1+}^{(3/2)}(Q^2) = \frac{|\mathbf{k}|}{m_N} \sqrt{\frac{3\alpha}{8\Gamma_{exp}q_R}} G_M^*(Q^2), \quad (24)$$

where  $\alpha = 1/137$  and  $\Gamma_{exp} = 115$  MeV. The best fit of the experimental data was provided with a parameter  $\gamma = 0.24$  (c/GeV) $^2$  in Eq. (21). In Fig. 15 we also show results obtained without additional unitarization for finite  $Q^2$ , i.e.  $\phi = \phi_R = \text{const}$ , independent of  $Q^2$ . In this case the real part of the  $M_{1+}^{(3/2)}$  multipole does not vanish at the resonance as soon as  $Q^2$  is finite (dotted curve).

Important information about  $D$ -state components of the nucleon and  $\Delta$  wave functions may be extracted from the study of the  $R_{EM} = E_{1+}/M_{1+}$  and  $R_{SM} = S_{1+}/M_{1+}$  ratios in the isospin 3/2 channel. In Fig. 15 we give our predictions for the  $Q^2$  dependence of these ratios at resonance. The ratios are practically constant in the non-unitarized case of  $\phi = \phi_R = \text{const}$  (dashed curves), because we assumed that the  $Q^2$  dependence of the  $E_{1+}$  and  $S_{1+}$  multipoles is the same as in the case of  $M_{1+}$ . However, this behaviour changes after unitarization, especially for  $Q^2 < 0.5$  (GeV/c) $^2$ .

Only little information is available on the multipole  ${}_p M_{1-}^{(1/2)}$  related to the excitation of the Roper resonance  $P_{11}(1440)$ . In our analysis as well as in many other ones, we neglect the contributions from longitudinal resonance excitations, because of a lack of any reliable data. Moreover, an analysis of the existing exclusive and inclusive

electroproduction data [39] showed no indication of an excitation of the Roper resonance at high  $Q^2$ . This implies a rapid fall-off of the corresponding proton helicity amplitude  $A_{1/2}$  with  $Q^2$ . However, such a result would be at variance with numerous quark model calculations.

Following Ref. [40] we take the  $Q^2$  dependence of the electromagnetic amplitude  ${}_p\bar{\mathcal{M}}_{1-}^{(1/2)}$  at resonance ( $W = 1440$  MeV) in the form

$${}_p\bar{\mathcal{M}}_{1-}^{(1/2)}(Q^2) = {}_p\bar{\mathcal{M}}_{1-}^{(1/2)}(0) \frac{|\mathbf{k}|}{k_W} \exp\left(-\frac{Q^2}{6\alpha^2}\right), \quad (25)$$

where  $\alpha$  is the harmonic oscillator parameter of quark model calculations whose value varies from  $\alpha = 0.229$  GeV, which reproduces the proton charge radius, to  $\alpha = 0.410$  GeV, which fits the  $A_{3/2}$  helicity amplitude for the  $D_{13}$  resonance [43]. Beyond the resonance peak we introduced an additional  $Q^2$  dependence in the form factor  $f_{\gamma N}$  using the usual prescription, replacing  $k_W \rightarrow |\mathbf{k}|$  and  $k_R \rightarrow \tilde{k}_R = |\mathbf{k}|_{W=W_R}$ .

Due to the importance of the inelastic channels, we can no longer apply the Fermi-Watson theorem to the  $P_{11}$  resonance as well as to resonances in the second and third resonance regions. As in the case of real photons we will assume that the real part of the multipoles vanishes at resonance, i.e.  $\psi(W_R) = \pi/2$  independent of  $Q^2$ . As a consequence of Eq. (14), the phase  $\phi$  becomes a  $Q^2$  dependent function. The procedure of finding  $\phi(Q^2)$  at resonance we will again call *unitarization procedure*.

As may be seen in Fig. 16, the application of the unitarization procedure to the  ${}_pM_{1-}^{(1/2)}$  multipole strongly modifies the original  $Q^2$  dependence defined by Eq. (25), leading to a rapid fall-off with  $Q^2$ . In the non-unitary approach, where  $\phi = \phi_R = \text{const}$ , the  $Q^2$  dependence is smoother and the real part of the  ${}_pM_{1-}^{(1/2)}$  multipole has a large negative value at resonance. In Fig. 16 we illustrate the effect of unitarization also for the proton helicity amplitude  $A_{1/2}$  which is related to the amplitude  ${}_p\bar{\mathcal{M}}_{1-}^{(1/2)}$  by

$$A_{1/2}(Q^2) = {}_p\bar{\mathcal{M}}_{1-}^{(1/2)}(Q^2) \cos \phi(Q^2). \quad (26)$$

For the harmonic oscillator parameter we have taken the value  $\alpha = 0.370$  GeV. With such a value our unitarization procedure works up to  $Q^2=1$  (GeV/c)<sup>2</sup>, while smaller values of  $\alpha$  limit applicability to smaller momentum  $Q^2$ .

The  $Q^2$  dependence of the pion electroproduction amplitudes in the second and third resonance regions has been defined in accordance with Refs. [14,44,45], where  $S_{11}(1535)$ ,  $D_{13}(1520)$ ,  $D_{33}(1700)$ , and  $F_{15}(1680)$  resonances are considered the dominant states of the  $[70, 1^-]_1$  and  $[56, 2^+]_2$  super multiplets in an  $SU(6) \otimes O(3)$  symmetry scheme. Within this model the transitions between the nucleon and its resonances are expressed in terms of the quark electric and magnetic multipoles  $e_\lambda^{LL}$  and  $m_\lambda^{LJ}$ , where  $\lambda$  is the photon helicity,  $L$  and  $J = L$  or  $L + 1$  are the orbital and total angular momenta, depending on the multipolarity of the transitions. As in most other analyses of the experimental data, we neglect the contributions from the longitudinal (or Coulomb) transitions assuming that the corresponding quark multipoles  $e_0^{LL}$  and  $m_0^{LL}$  vanish.

Our choice to express the  $Q^2$  dependence in terms of the quark multipole moments is motivated, first, by their simple connection with the amplitudes  $\bar{A}_{l\pm}$  listed in Table 5. Second, as we will see below, the quark multipole moments exhibit a very simple  $Q^2$  dependence. The third advantage is that by this way we can obtain both proton and neutron amplitudes. As may be seen in Table 5 we have assumed a certain deviation from the predictions of the  $SU(6)$  symmetry in the case of the neutron amplitudes in order to match with our values for the corresponding helicity amplitudes at the photon point, leading to a 10% increase for the  $D_{13}(1520)$ , a 10% decrease for the  $F_{15}(1680)$  and 30% decrease for the  $S_{11}(1535)$  resonances.

In terms of the quark multipoles the experimental data have been compiled by Burkert et al. [41,44] in the form

$$e_1^{11} = \tilde{e}_1^{11} F_D(Q_{EVF}^2), \quad m_1^{1J} = \tilde{m}_1^{1J} F_D(Q_{EVF}^2) \quad (27)$$

for the transition to the  $[70, 1^-]_1$  super multiplet describing the excitation of the  $S_{11}(1535)$ ,  $D_{13}(1520)$  and  $D_{33}(1700)$  resonances, and

$$e_1^{22} = \tilde{e}_1^{22} Q_{EVF} F_D(Q_{EVF}^2), \quad m_1^{2J} = \tilde{m}_1^{2J} Q_{EVF} F_D(Q_{EVF}^2) \quad (28)$$

for the transition to the  $[56, 2^+]_2$  super multiplet describing the excitation of the  $F_{15}(1680)$  resonance. In order to minimize relativistic effects, the  $Q^2$  dependence is evaluated in the equal velocity frame (EVF) with

$$Q_{EVF}^2 = \frac{(W_R^2 - m_N^2)^2}{4m_N W_R} + Q^2 \frac{(W_R + m_N)^2}{4m_N W_R}, \quad F_D(Q_{EVF}^2) = \frac{1}{(1 + Q_{EVF}^2/0.71)^2}. \quad (29)$$

The  $Q^2$  dependence of the so-called *reduced quark multipole moments*  $\tilde{e}_1^{LL}$  and  $\tilde{m}_1^{LJ}$  is parametrized similarly as in Ref. [45] with a slight modification in order to match with the amplitudes  $\bar{\mathcal{A}}_{l\pm}$  of Table 3 (or the helicity amplitudes of Table 4) at the photon point. For the transition to the  $[70, 1^-]_1$  super multiplet we obtain

$$\begin{aligned}\tilde{e}_1^{11} &= 2.56, \quad \tilde{m}_1^{11} = 1.80 - 3.93 Q_{EVF}^2, \\ \tilde{m}_1^{12} &= \begin{cases} -0.42 + 5.82 Q_{EVF}^2, & Q_{EVF}^2 \leq 1.0 \text{ GeV}^2 \\ 5.84 - 0.44 Q_{EVF}^2, & Q_{EVF}^2 > 1.0 \text{ GeV}^2 \end{cases}.\end{aligned}\quad (30)$$

For the transition to the  $[56, 2^+]_1$  super multiplet the parametrization is

$$\begin{aligned}\tilde{e}_1^{22} &= 4.35, \quad \tilde{m}_1^{22} = 3.823 - 4.172 Q_{EVF}^2, \\ \tilde{m}_1^{23} &= \begin{cases} 0.42 + 5.1 Q_{EVF}^2, & Q_{EVF}^2 \leq 1.0 \text{ GeV}^2 \\ 6.31 - 0.79 Q_{EVF}^2, & Q_{EVF}^2 > 1.0 \text{ GeV}^2 \end{cases}.\end{aligned}\quad (31)$$

Note that in Eqs. (30-31)  $Q_{EVF}$ ,  $\tilde{e}^{1J}$  and  $\tilde{m}^{1J}$  are given in GeV,  $\tilde{e}^{2J}$  and  $\tilde{m}^{2J}$  are dimensionless. In Figs. 17 and 18 we demonstrate the consistency of our parametrization with the reduced quark multipole moments and helicity amplitudes compiled by Burkert [41,44]. Note that for the second  $S_{11}(1650)$  resonance we followed the assumption of Ref. [45],

$$A_{1/2}^{S_{11}(1650)}(Q^2) = A_{1/2}^{S_{11}(1535)}(Q^2) \tan 30^\circ, \quad (32)$$

where the  $30^\circ$  mixing angle matches our value for the helicity amplitude at the photon point.

The unitarization procedure for the excitation of the  $D_{13}(1520)$ ,  $D_{33}(1700)$  and  $F_{15}(1680)$  resonances is similar to the procedure for the  $P_{11}(1440)$  resonance, i.e. we assume that the total phase  $\psi = \pi/2$  at  $W = W_R$  is independent of  $Q^2$ . In Fig. 19 we compare the  $Q^2$  dependence for the more important proton electric and magnetic multipoles at resonance to the results of the analyses from DESY, NINA and Bonn, compiled by Foster and Hughes [39]. In contrast to the case of the  $P_{11}$  resonance, our unitarization procedure for these multipoles does not seriously modify the original  $Q^2$  dependence of the quark multipole moments, as can be seen by comparing the solid and dashed curves in Fig. 19.

In the following Figs. 20-23 we present some examples for observables of  $\pi^+$  and  $\pi^0$  electroproduction. In general the results of our model are in good agreement with the existing data. In particular we note that our results obtained without  $P_{11}(1440)$  resonance contribution get closer to the data with increasing  $Q^2$ . This indicates a strong decrease of  $A_{1/2}(P_{11})$  as function of  $Q^2$ . We hope that future experimental studies will clarify these problems occurring for the Roper resonance contribution. Furthermore a precise  $L/T$  separation would be very useful in order to obtain more information about the  $Q^2$  dependence of the  $S_{1-}$  multipoles.

Finally, we comment on the  $u$ -channel resonances which are often present in effective Lagrangian approaches. Obviously, the main subject of experimental and theoretical studies are the  $s$ -channel resonances, while the contributions from the tails of the  $u$ -channel resonances are just slowly varying backgrounds which are essentially real and affect all the multipoles. We assume that the  $u$ -channel contributions are effectively included in the unitarization procedure and the nonresonant background of our model. More sophisticated methods beyond the isobar model of our work will demand an explicit inclusion of the  $u$ -channel resonances in a crossing symmetric way.

## VI. CONCLUSION

We have developed a new operator for pion photo- and electroproduction for applications to reactions on nuclei at photon equivalent energies up to 1 GeV. The model contains Born terms, vector mesons and nucleon resonances up to the third resonance region ( $P_{33}(1232)$ ,  $P_{11}(1440)$ ,  $D_{13}(1520)$ ,  $S_{11}(1535)$ ,  $F_{15}(1680)$ , and  $D_{33}(1700)$ ).

For the Born terms we propose an energy dependent superposition of pseudovector and pseudoscalar  $\pi NN$  couplings. This procedure describes the correct energy dependence of the nonresonant multipoles for photon *lab* energies up to  $E_\gamma = 1$  GeV, in particular in the case of the  $E_{0+}^{3/2}$  and  $M_{1-}^{3/2}$  multipoles, and provides an excellent agreement with the results of the Mainz multipole analysis at photon energies below 500 MeV and with the VPI analysis at higher energies.

The resonance contributions in the  $s$ -channel are parametrized by the standard Breit-Wigner form for the relevant multipoles. Unitarity is fulfilled by multiplying the resonance terms with appropriate phases. We find that the unitarization procedure developed for pion electroproduction is very important for extracting the  $M_{1+}^{(3/2)}$ ,  $E_{1+}^{(3/2)}$  and  $L_{1+}^{(3/2)}$  resonance multipoles, especially for small  $Q^2$ . In the case of the  $P_{11}(1440)$  resonance, we assume that the phase

of the total  ${}_p M_{1-}^{(1/2)}$  multipole is independent of  $Q^2$  at resonance which leads to a suppression of the Roper resonance with increasing values of  $Q^2$ .

The  $Q^2$  dependence of the electromagnetic form factors for the  $S_{11}$ ,  $D_{13}$ ,  $D_{33}$ , and  $F_{15}$  resonances is expressed in terms of quark multipole moments, attributing the first three states to the  $[70, 1^-]$  and the last state to the  $[50, 2^+]$  multiplets. The assumption of a  $Q^2$  independent phase at resonance leads only to a small modification of the  $Q^2$  dependence of the helicity amplitudes in these cases.

Within our model we obtain good agreement with the existing experimental data for pion photo- and electroproduction on the nucleon. Due to its inherent simplicity, the model is well adopted for predictions and analysis of future results on pion electroproduction on nucleons and nuclei.

## ACKNOWLEDGMENTS

We would like to thank R. Beck, R. W. Gothe, H. Schmieden and B. Schoch for helpful discussions. S.S.K. is grateful to the Theory group for the hospitality extended to him during his stay at the University of Mainz. This work was supported by the Deutsche Forschungsgemeinschaft (SFB 201).

## APPENDIX:

In this appendix, we give the  $W$  and  $Q^2$  dependence for the phases  $\phi$  in the Breit-Wigner parametrization obtained after the unitarization procedure. First, let us consider the  $W$  dependence at the photon point  $Q^2=0$ . In this case our results for the phases of the magnetic, electric and longitudinal components of the  $P_{33}(1232)$  resonance can be parametrized by

$$\begin{aligned}\phi_M(0) &= 22.130x - 3.769x^2 + 0.184x^3, \\ \phi_E(0) &= 83.336x - 28.457x^2 + 3.356x^3 - 0.122x^4, \\ \phi_L(0) &= 43.668x - 2.872x^2 - 1.910x^3 + 0.230x^4,\end{aligned}\quad (\text{A1})$$

where  $x = (W - m_\pi - m_N)/(100 \text{ MeV})$ . All phases are given in degrees.

For the phases of the proton and neutron components of the magnetic excitation of the  $P_{11}(1440)$  resonance we have

$$\begin{aligned}\phi_p(0) &= -4.661x + 0.349x^2 - 0.240x^3, \\ \phi_n(0) &= -22.935x + 19.935x^2 - 4.456x^3 + 0.048x^4 + 0.039x^5.\end{aligned}\quad (\text{A2})$$

The longitudinal excitation of the Roper resonance is neglected in our model. For the other resonances we assumed the phases  $\phi$  to be constants as listed in Table 3.

The  $Q^2$  dependence of  $\phi$  is parametrized as

$$\phi(Q^2) = \frac{1 + AQ^2}{1 + BQ^2} \phi(0). \quad (\text{A3})$$

The coefficients  $A$  and  $B$  for the  $P_{33}(1232)$  resonance depend on  $W$  and are given in Table 6. With good accuracy the phases of all other resonances can be taken as constants, identical for proton and neutron. The corresponding values for these phases are given in Table 7. Note that for the  $S_{11}$  and  $D_{33}$  resonances we take  $A = B = 0$ .

- [1] D. Drechsel and L. Tiator, J. Phys. G: Nucl. Phys. **18** (1992) 449
- [2] S. Mehrotra, L.E. Wright, Nucl. Phys. **A362** (1981) 461
- [3] R. Davidson, N. C. Mukhopadhyay and R. Wittman, Phys. Rev. **D43** (1991) 71
- [4] S. Nozawa, B. Blankleider and T.-S. H. Lee, Nucl. Phys. **A513** (1990) 459; S. Nozawa and T.-S. Lee, Nucl. Phys. **A513** (1990) 511
- [5] A. Gil, J. Nieves and E. Oset, Nucl. Phys. **A627** (1997) 543; R. C. Carrasco and E. Oset, Nucl. Phys. **A536** (1992) 445

[6] H. Garcilazo, E. Moya de Guerra, Nucl. Phys. **A562** (1993) 521  
[7] , M. Guidal, J.M. Laget, and M. Vanderhaeghen, Nucl. Phys. **A627** (1997) 625  
[8] T. Feuster and U. Mosel, **nucl-th/9803057**  
[9] I. Blomqvist and J. M. Laget, Nucl. Phys. **A280** (1977) 405  
[10] R. A. Arndt, I. I. Strakovsky and R. L. Workman, Phys. Rev. **C53** (1996) 430 (SP97 solution of the VPI analysis)  
[11] O. Hanstein, D. Drechsel, and L. Tiator, Nucl. Phys. **A632** (1998) 561  
[12] R. L. Walker, Phys. Rev. **182** (1969) 1729  
[13] R. D. Moorehouse, in A. Donnachie and Shaw, *Electromagnetic Interactions of Hadrons*, N.Y. (1978)  
[14] W. N. Cottingham and I. H. Dunbar, Z. Phys. **C2** (1979) 41  
[15] M. G. Olsson, Nucl. Phys. **B78** (1974) 55  
[16] J. M. Laget, Nucl. Phys. **A481** (1988) 765  
[17] G. Knöchlein, D. Drechsel and L. Tiator, Z. Phys. **A352** (1995) 327  
[18] G. F. Chew, M. L. Goldberger, F. E. Low, and Y. Nambu, Phys. Rev. **106** (1957) 1345  
[19] F. A. Berends, A. Donnachie and D. L. Weaver, Nucl. Phys. **B4** (1967) 1  
[20] O. Dumbrăjs it et al., Nucl. Phys. **B216** (1983) 277  
[21] A. I. L'vov, V. A. Petrun'kin and M. Schumacher, Phys. Rev. **C55** (1997) 359  
[22] R. A. Arndt, R. L. Workman, Zh. Li and L. D. Roper, Phys. Rev. **C42** (1990) 1864  
[23] D. Schwela and W. Weizel, Z. Phys. **221** (1969) 71  
[24] Particle Data Group, Phys. Rev. **D54** (1996) 1  
[25] G. Fischer et al., Z. Phys. **253** (1972) 38  
[26] K. Buechler et al., Nucl. Phys. **A570** (1994) 580  
[27] H. Dutz, et al., Nucl. Phys. **A601** (1994) 319  
[28] R. Beck et al., Phys. Rev. Lett. **78** (1997) 606; H.-P. Krahn, Ph.D thesis, Mainz (1996); F. Haerter, Ph.D thesis, Mainz (1996)  
[29] B. Zucht, Ph.D thesis, Bonn (1995); D. Krämer, Ph.D thesis, Bonn (1993)  
[30] K. H. Althoff et al., Z. Phys. **C18** (1983) 199  
[31] C. Betourne et al., Phys. Rev. **172** (1968) 1343  
[32] S. D. Ecklund and R. L. Walker, Phys. Rev. **159** (1967) 1195  
[33] H. W. Dannhausen, Preprint Bonn, 1977, IR-77-29  
[34] M. Yoshioka et al., Nucl. Phys. **B168** (1980) 222  
[35] D. Menze, W. Pfeil and R. Wilcke. Compilation of pion photoproduction data, Physikalisches Institut der Universität Bonn, 1977  
[36] P. J. Bussey et al., Nucl. Phys. **B154** (1979) 205  
[37] G. Knies et al., Phys. Rev. **D10** (1974) 2778  
[38] V. B. Ganenko et al., Sov. J. Nucl. Phys. **23** (1976) 100  
[39] F. Foster and G. Hughes, Rep. Prog. Phys. **46** (1983) 1445  
[40] Z. P. Li, V. Burkert and Zh. Li, Phys. Rev **D46** (1992) 1570  
[41] V. Burkert, Proc. of the Topical Workshop on "Excited Baryons 1988", Troy, New York (1988), eds. G. Adams, N. Mukhopadhyay and P. Stoler, World Scientific, Singapore (1989), p. 122  
[42] V. Burkert, CEBAF proposal PR-93-035 (1993)  
[43] M. Aiello, M. M. Giannini, E. Santopinto, J. Phys. **G24** (1998) 753  
[44] H. Breuker, et al., Z. Phys. **C17** (1983) 121  
[45] V. Burkert and Zh. Li, CEBAF proposal PR-92-017 (1992)  
[46] S. Stein et al., Phys. Rev. **D12** (1975) 1884  
[47] W. Bartel et al., Phys. Lett. **28B** (1968) 148  
[48] R. Siddle et al., Nucl. Phys. **B35** (1971) 93  
[49] J. C. Alder et al., Nucl. Phys. **B46** (1972) 573  
[50] F. Kalleicher et al., Z. Phys. **A359** (1997) 201  
[51] H. Breuker et al., Nucl. Phys. **B146** (1978) 285

	$m_V$ [MeV]	$\lambda_V$	$\tilde{g}_{V1}$	$\tilde{g}_{V2}/\tilde{g}_{V1}$	$\Lambda_V$ [GeV]
$\omega$	782.6	0.314	21	-0.57	1.2
$\rho$	769.0	0.103	2.	6.5	1.5

TABLE I. Masses and coupling constants for the vector mesons.

$N^*$	$W_R$ [MeV]	$\Gamma_R$ [MeV]	$\beta_\pi$	Multipoles
$P_{33}(1232)$	1235	130	1.0	$E_{1+}^{(3/2)}, M_{1+}^{(3/2)},$
$P_{11}(1440)$	1440	350	0.70	$p,n M_{1-}^{(1/2)}$
$D_{13}(1520)$	1520	130	0.60	$p,n E_{2-}^{(1/2)}, p,n M_{2-}^{(1/2)}$
$S_{11}(1535)$	1520	80	0.40*)	$p,n E_{0+}^{(1/2)}$
$S_{11}(1650)$	1690	100	0.85	$p,n E_{0+}^{(1/2)}$
$F_{15}(1680)$	1680	135	0.70	$p,n E_{3-}^{(1/2)}, p,n M_{3-}^{(1/2)}$
$D_{33}(1700)$	1740	450	0.15	$E_{2-}^{(3/2)}, M_{2-}^{(3/2)},$

TABLE II. Parameters of nucleon resonances. \*) The branching ratios for the eta and two-pion decay channels are 50% and 10%, respectively.

$N^*$	$\mathcal{A}_{l\pm}$	$\phi_R$	$\mathcal{A}_{l\pm}$ (proton)	$\mathcal{A}_{l\pm}$ (neutron)	$n$
$P_{33}(1232)$	$\bar{\mathcal{M}}_{1+}^{(3/2)}$	26	323	323	2
	$\bar{\mathcal{E}}_{1+}^{(3/2)}$	73	-17	-17	1
$P_{11}(1440)$	$p,n \bar{\mathcal{M}}_{1-}^{(1/2)}$	-25	-78	66	1
$D_{13}(1520)$	$p,n \bar{\mathcal{E}}_{2-}^{(1/2)}$	23	-145	149	2
	$p,n \bar{\mathcal{M}}_{2-}^{(1/2)}$	35	-68	23	4
$S_{11}(1535)$	$p,n \bar{\mathcal{E}}_{0+}^{(1/2)}$	0	-67	55	3
$S_{11}(1650)$	$p,n \bar{\mathcal{E}}_{0+}^{(1/2)}$	0	-39	32	4
$F_{15}(1680)$	$p,n \bar{\mathcal{E}}_{3-}^{(1/2)}$	15	-64	7.7	3
	$p,n \bar{\mathcal{M}}_{3-}^{(1/2)}$	15	-37	22	4
$D_{33}(1700)$	$\bar{\mathcal{E}}_{2-}^{(3/2)}$	61	-240	-240	4
	$\bar{\mathcal{M}}_{2-}^{(3/2)}$	61	38	38	4

TABLE III. Unitary phases  $\phi_R$  at the resonance position (in deg) and electromagnetic amplitudes  $\bar{\mathcal{A}}_{l\pm}$  (in  $10^{-3} GeV^{-1/2}$ ),  $n$  is the parameter in Eq. (18).

$N^*$		$A_{1/2}(\text{proton})$	$A_{3/2}(\text{proton})$	$A_{1/2}(\text{neutron})$	$A_{3/2}(\text{neutron})$
$P_{33}(1232)$	our	-138	-256	-138	-256
	PDG	-140 $\pm$ 5	-258 $\pm$ 6	-140 $\pm$ 5	-258 $\pm$ 6
$P_{11}(1440)$	our	-71	—	60	—
	PDG	-65 $\pm$ 4	—	40 $\pm$ 10	—
$D_{13}(1520)$	our	-17	164	-40	-135
	PDG	-24 $\pm$ 9	166 $\pm$ 5	-59 $\pm$ 9	-139 $\pm$ 11
$S_{11}(1535)$	our	67	—	-55	—
	PDG	70 $\pm$ 12	—	-46 $\pm$ 27	—
$S_{11}(1650)$	our	39	—	-32	—
	PDG	53 $\pm$ 16	—	-15 $\pm$ 21	—
$F_{15}(1680)$	our	-10	138	35	-41
	PDG	-15 $\pm$ 6	133 $\pm$ 12	29 $\pm$ 10	-33 $\pm$ 9
$D_{33}(1700)$	our	86	85	86	85
	PDG	104 $\pm$ 15	85 $\pm$ 22	104 $\pm$ 15	85 $\pm$ 22

TABLE IV. Helicity amplitudes (in  $10^{-3} \text{GeV}^{-1/2}$ ).

$N^*$	multiplet	$\mathcal{A}_{l\pm} C_R \cos \phi_R$	proton	neutron
$D_{13}(1520)$	[70, 1 $^-$ ]	${}_{p,n}\bar{\mathcal{E}}_{2-}^{(1/2)} C_R \cos \phi_R$	$-\sqrt{2}e^{11} - m^{11}$	$1.1(\sqrt{2}e^{11} + \frac{1}{3}m^{11})$
		${}_{p,n}\bar{\mathcal{M}}_{2-}^{(1/2)} C_R \cos \phi_R$	$-m^{12}$	$\frac{1}{3}m^{12}$
$S_{11}(1535)$	[70, 1 $^-$ ]	${}_{p,n}\bar{\mathcal{E}}_{0+}^{(1/2)} C_R \cos \phi_R$	$-e^{11} + \sqrt{2}m^{11}$	$0.7(e^{11} - \sqrt{\frac{2}{9}}m^{11})$
$F_{15}(1680)$	[56, 2 $^+$ ]	${}_{p,n}\bar{\mathcal{E}}_{3-}^{(1/2)} C_R \cos \phi_R$ ${}_{p,n}\bar{\mathcal{M}}_{3-}^{(1/2)} C_R \cos \phi_R$	$-\sqrt{\frac{3}{5}}e^{22} - \sqrt{\frac{2}{5}}m^{22}$ $-\sqrt{\frac{1}{2}}m^{23}$	$0.9\sqrt{\frac{8}{45}}m^{22}$ $0.9\sqrt{\frac{2}{9}}m^{23}$
$D_{33}(1700)$	[70, 1 $^-$ ]	${}_{p,n}\bar{\mathcal{E}}_{2-}^{(3/2)} C_R \cos \phi_R$ ${}_{p,n}\bar{\mathcal{M}}_{2-}^{(3/2)} C_R \cos \phi_R$	$-\sqrt{2}e^{11} + \frac{1}{3}m^{11}$ $\frac{1}{3}m^{12}$	$-\sqrt{2}e^{11} + \frac{1}{3}m^{11}$ $\frac{1}{3}m^{12}$

TABLE V. Electromagnetic amplitudes  $\bar{\mathcal{A}}_{l\pm} C_R \cos \phi_R$ , where  $C_R = \frac{2}{e}\sqrt{3m_N(W_R^2 - m_N^2)}$ . Fourth and fifth column: these amplitudes expressed in terms of the quark multipole moments, for proton and neutron respectively.

multipoles	$M_{1+}^{(3/2)}$		$E_{1+}^{(3/2)}$		$L_{1+}^{(3/2)}$	
	A	B	A	B	A	B
$W(\text{MeV})$						
1100	1.500	3.859	5.377	27.29	1.802	19.64
1150	1.227	2.794	4.070	15.65	1.825	10.75
1200	0.9147	2.175	3.036	10.25	1.422	6.739
1250	0.8444	1.762	2.800	7.886	1.393	4.587
1300	0.8320	1.456	2.490	5.252	1.267	2.991
1350	0.7810	1.225	2.046	3.262	0.9363	1.715
1400	0.7277	1.045	1.775	2.239	0.5052	0.7424
1450	0.6815	0.9035	1.633	1.720	0.3361	0.3500
1500	0.6471	0.7963	1.604	1.500	0.2979	0.2100

TABLE VI. The coefficients A and B for the  $P_{33}(1232)$  resonance (in  $\text{GeV}^{-2}$ ).

A and B	${}_p M_{1-}^{(1/2)}$	${}_p E_{2-}^{(1/2)}$	${}_p M_{2-}^{(1/2)}$	${}_p E_{3-}^{(1/2)}$	${}_p M_{3-}^{(1/2)}$
A	9.977	15.17	1.563	-0.070	-1.024
B	2.384	21.98	5.202	3.766	3.938

TABLE VII. The coefficients A and B for the  $P_{11}(1440)$ ,  $D_{13}(1520)$  and  $F_{15}(1680)$  resonances (in  $GeV^{-2}$ ).

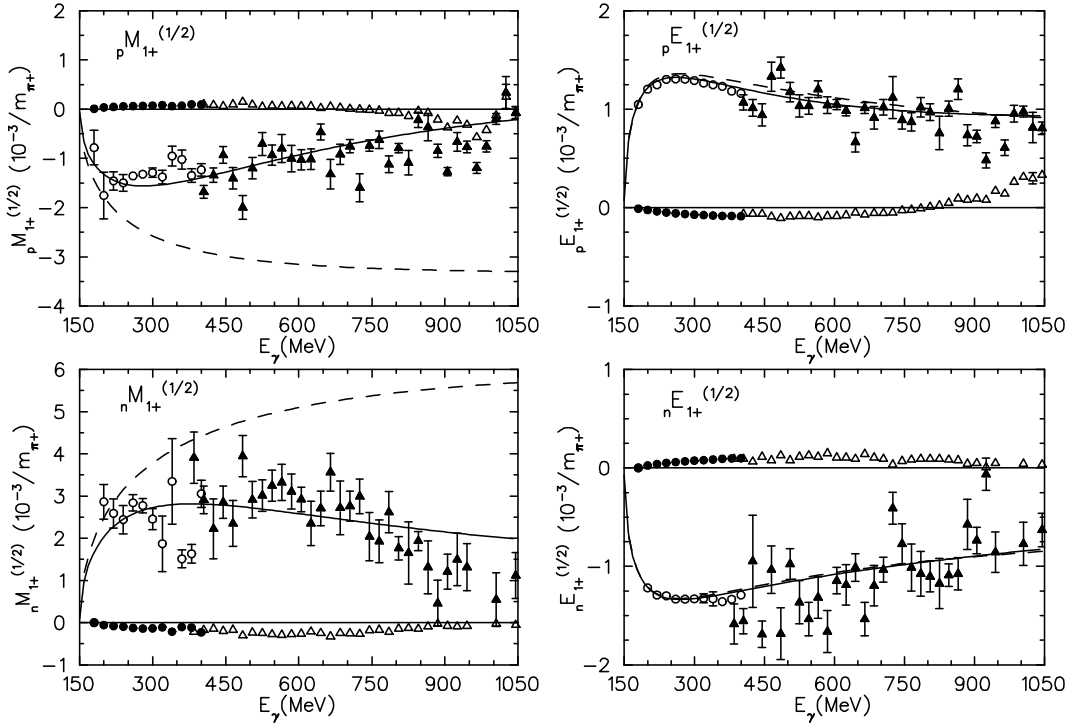


FIG. 1. Nonresonant multipoles  $p, n M_{1+}^{(1/2)}$  and  $p, n E_{1+}^{(1/2)}$  calculated without (dashed curves) and with (solid curves) vector meson contributions. The  $\pi NN$  coupling constant is taken as  $g^2/4\pi = 14.28$  and the coupling constants for the vector mesons are given in Table 1. The open and full circles are the real and imaginary parts from the Mainz dispersion analysis [11]. The full and open triangles are real and imaginary parts from the VPI analysis [10].

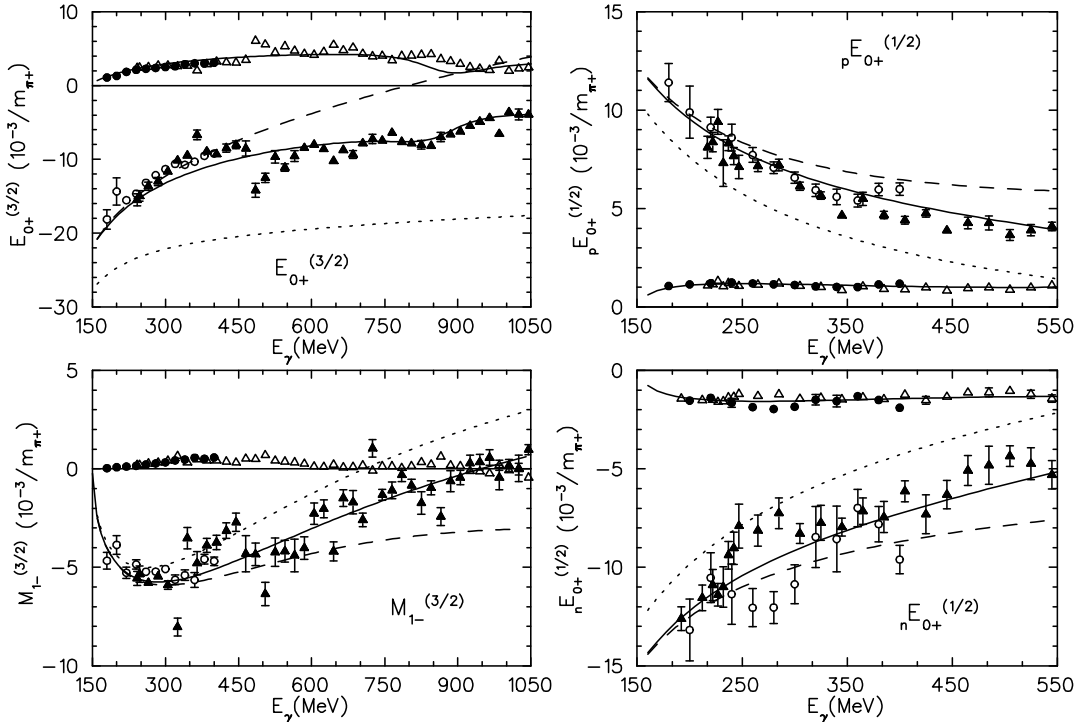


FIG. 2. Nonresonant  $E_{0+}$  and  $M_{1-}$  multipoles calculated with pure pseudovector (dashed curves) and pure pseudoscalar (dotted curves)  $\pi NN$  couplings. The solid curves are the results for the real and imaginary parts obtained using the Lagrangian (12) and the unitarization ansatz (13). Data points as in Fig. 1.

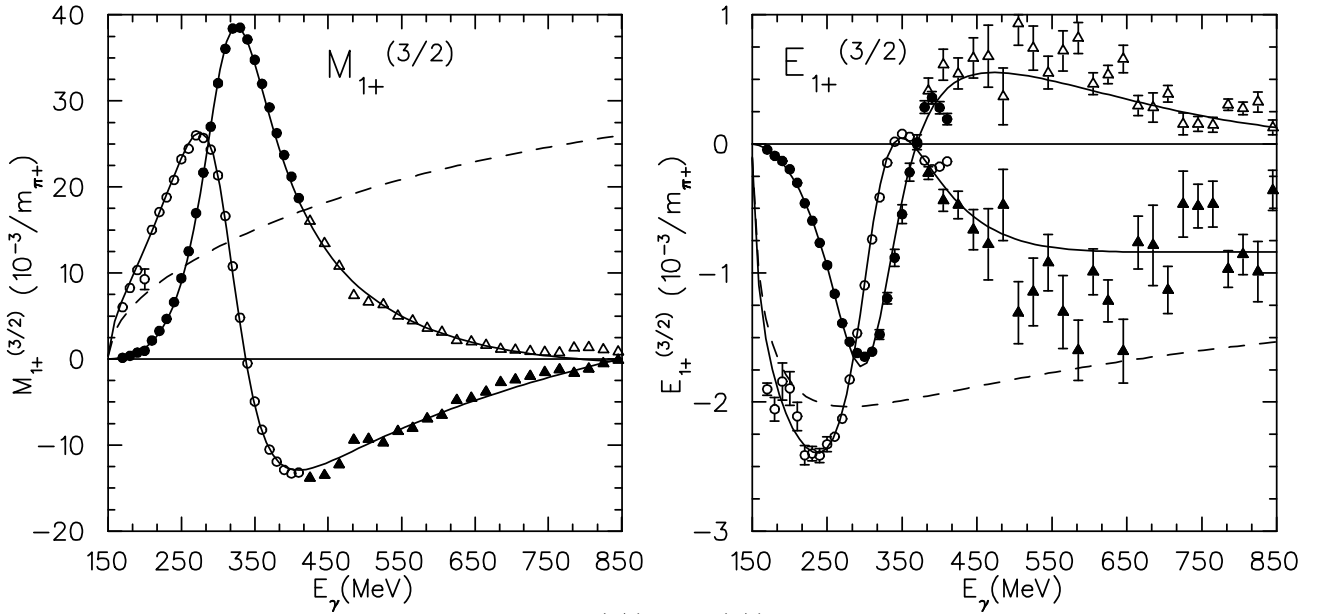


FIG. 3. Real and imaginary parts of the unitarized  $M_{1+}^{(3/2)}$  and  $E_{1+}^{(3/2)}$  multipoles (solid curves). The dashed curves are the  $\text{Born} + \omega, \rho$  contributions. Data points as in Fig. 1.

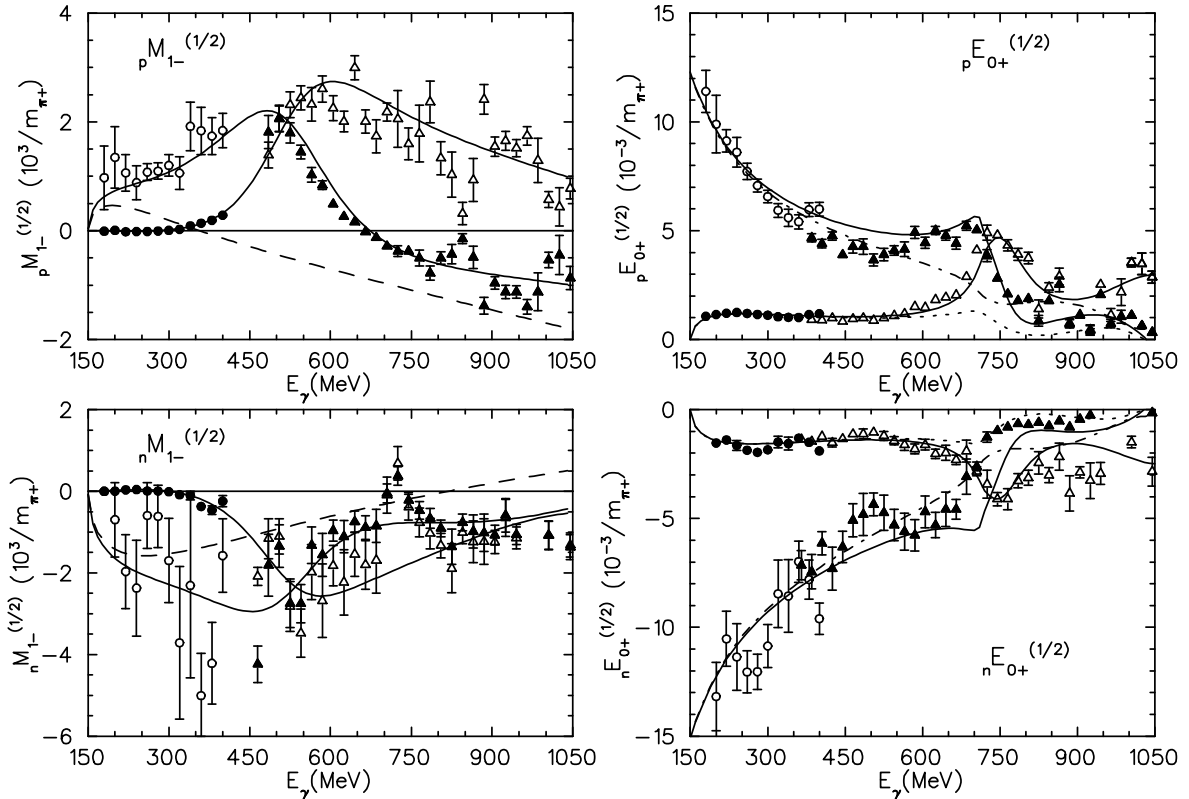


FIG. 4. The multipoles  $p,n M_{1-}^{(1/2)}$  and  $p,n E_{0+}^{(1/2)}$  calculated with the  $P_{11}(1440)$ ,  $S_{11}(1535)$  and  $S_{11}(1650)$  resonances. The dashed curves for the  $p,n M_{1-}^{(1/2)}$  multipoles are the  $\text{Born} + \omega, \rho$  contributions with our Lagrangian (12). The real (dash-dotted curve) and imaginary (dotted curve) parts of the  $p,n E_{0+}^{(1/2)}$  multipoles are obtained without the  $S_{11}$  resonances using the Lagrangian (12) and Eq. (13). Data points as in Fig. 1.

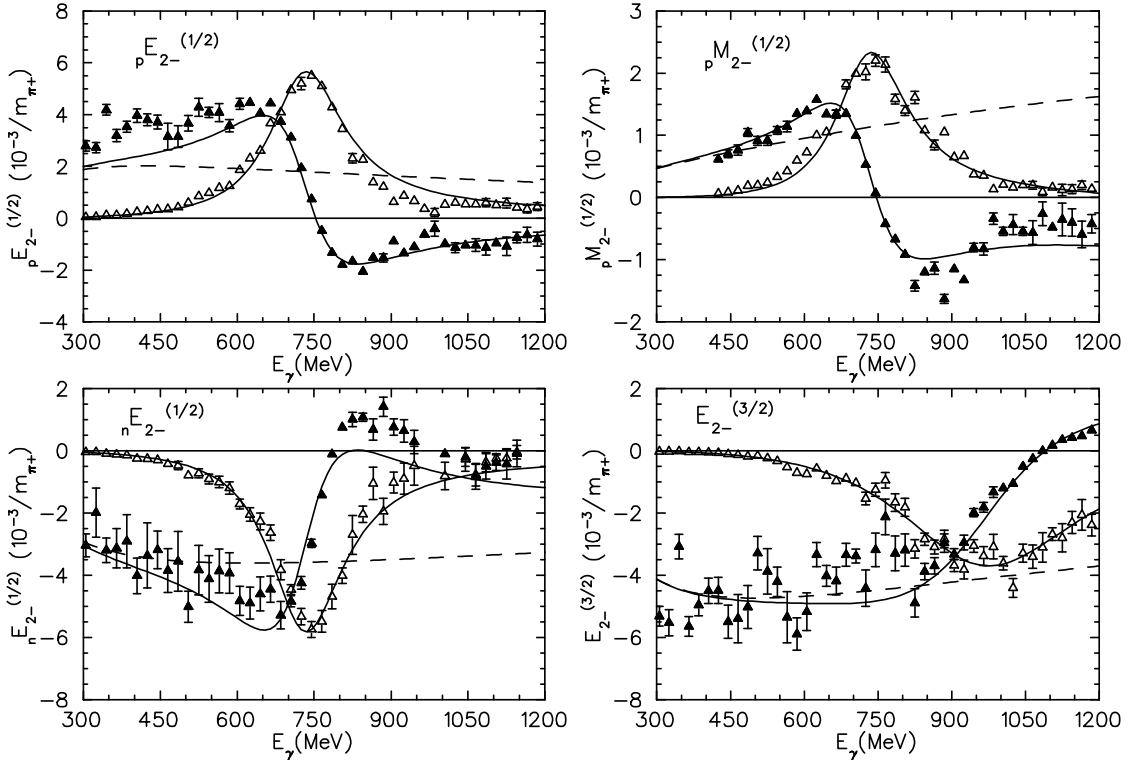


FIG. 5. The multipoles  $E_{2-}$  and  $M_{2-}$  calculated with the  $D_{13}(1520)$  and  $D_{33}(1700)$  resonance contributions. The dashed curves are the  $Born + \omega, \rho$  contributions. The full and open triangles are the real and imaginary parts from the VPI analysis [10].

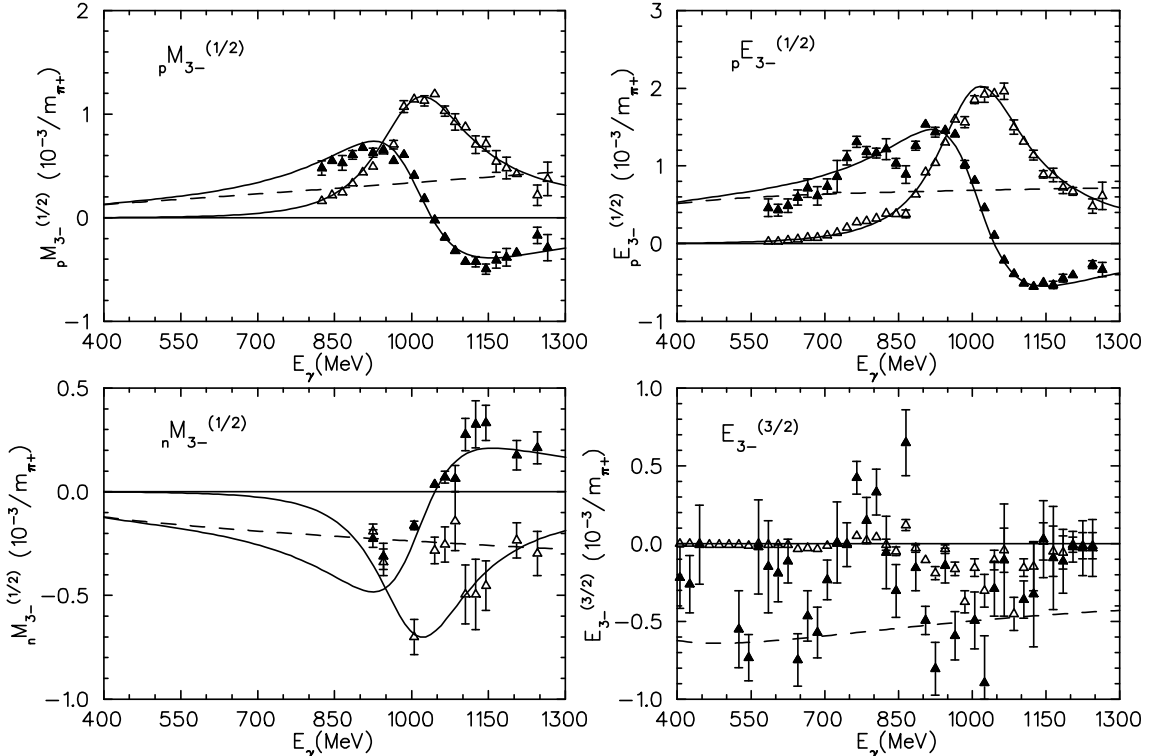


FIG. 6. The multipoles  $E_{3-}$  and  $M_{3-}$  calculated with the  $F_{15}(1680)$  resonance contributions. The dashed curves are the  $Born + \omega, \rho$  contributions. The full and open triangles are the real and imaginary parts from the VPI analysis [10].

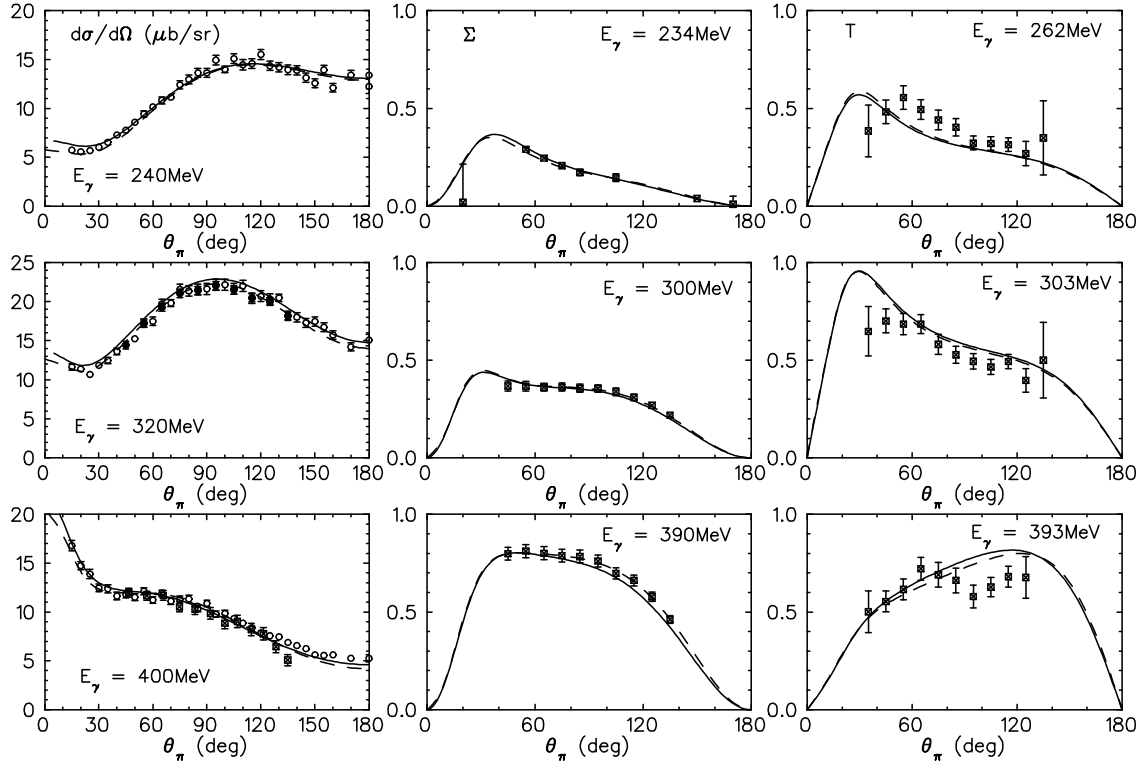


FIG. 7. Differential cross sections, photon ( $\Sigma$ ) and target ( $T$ ) asymmetries for  $p(\gamma, \pi^+)n$  in the first resonance region. The solid and dashed curves are the results of our calculations and the Mainz dispersion analysis [11], respectively. Experimental data from Refs. [25–27].

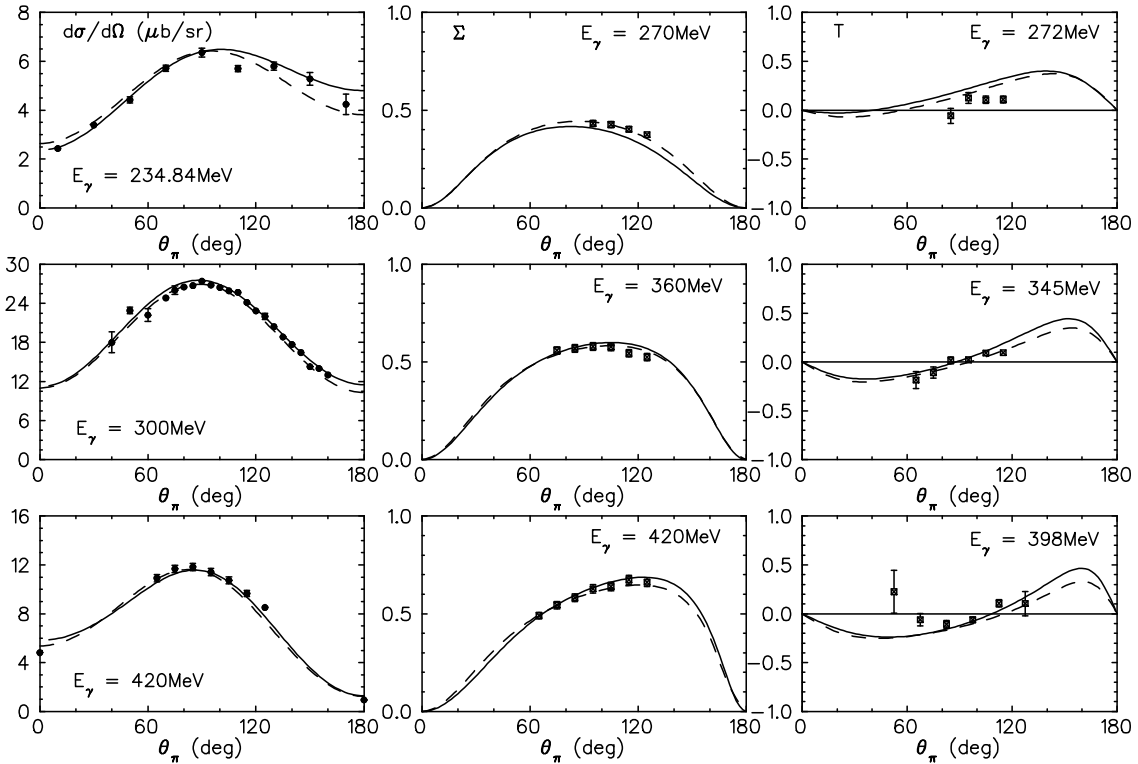


FIG. 8. The same as in Fig. 7 for  $p(\gamma, \pi^0)p$ . Experimental data from Refs. [28,29].

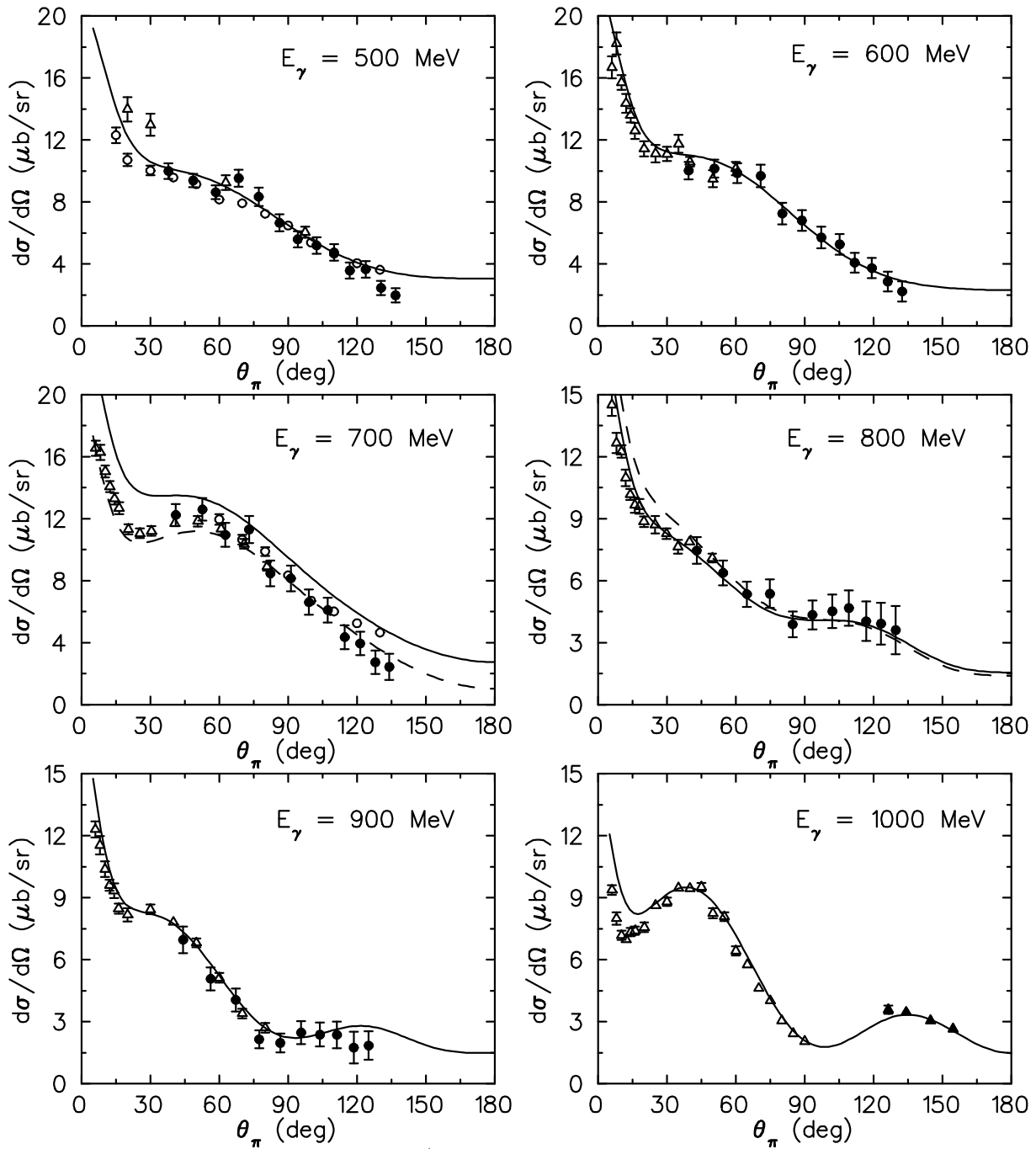


FIG. 9. Differential cross sections for  $p(\gamma, \pi^+)n$ . The dashed curves at  $E_\gamma = 700$  and 800 MeV are the results obtained without the  $S_{11}(1535)$  resonance. Experimental data from Refs. [26,30–33].

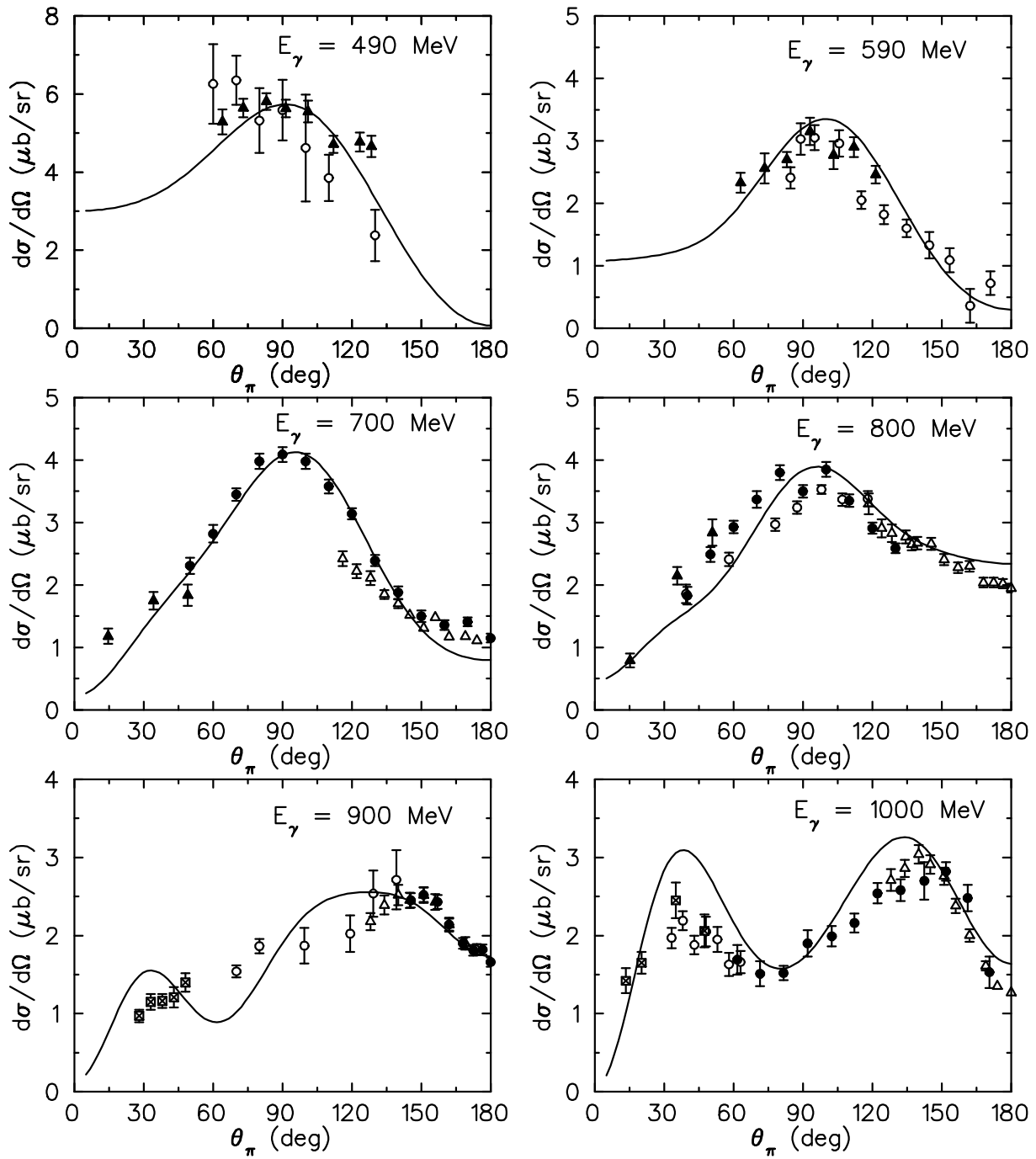


FIG. 10. Differential cross sections for  $p(\gamma, \pi^0)p$ . Experimental data from Refs. [34,35].

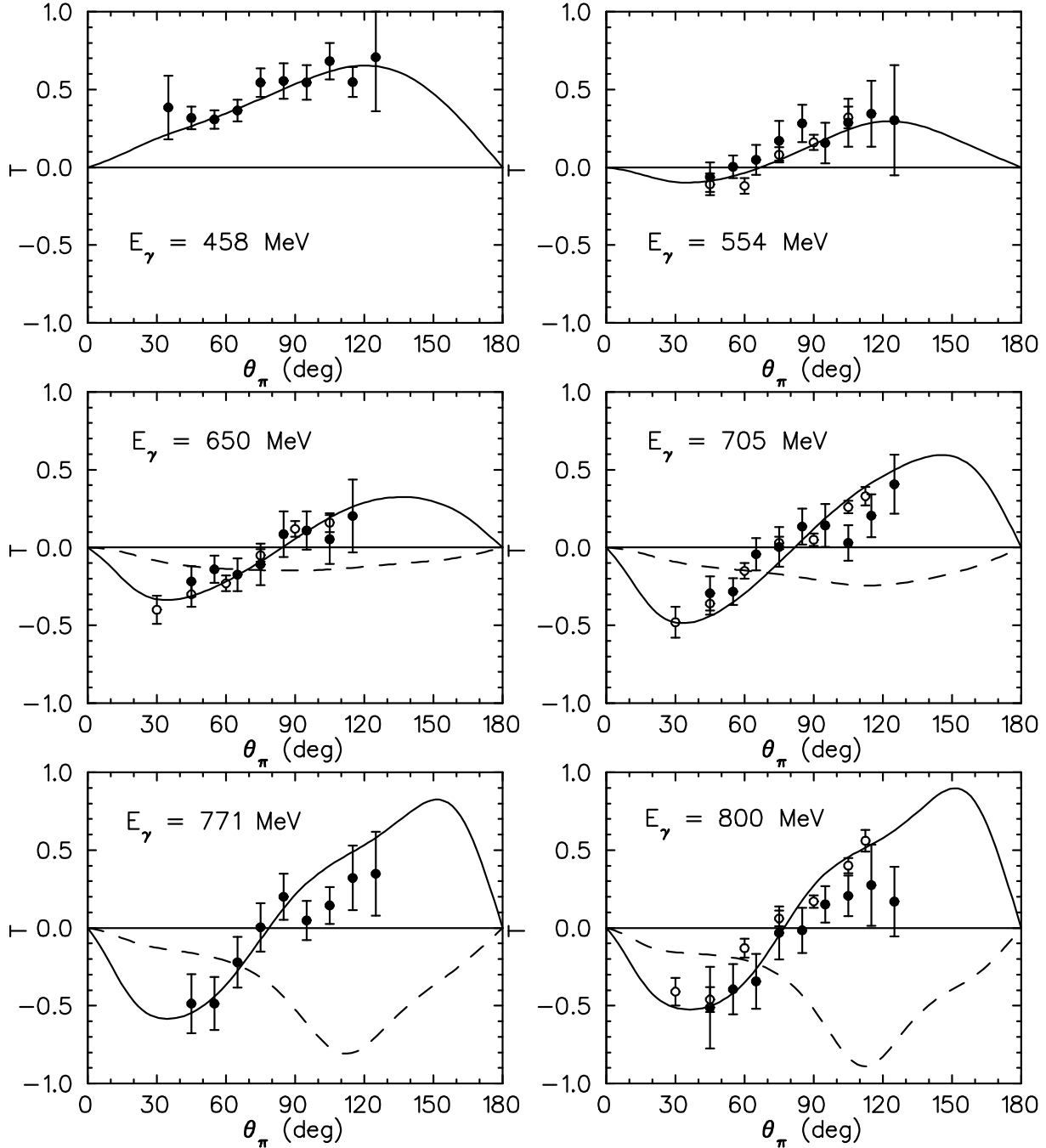


FIG. 11. Target asymmetries  $T$  for  $p(\gamma, \pi^+)n$ . The dashed curves are the results obtained without the  $D_{13}(1520)$  resonance. Experimental data from Refs. [27,36].

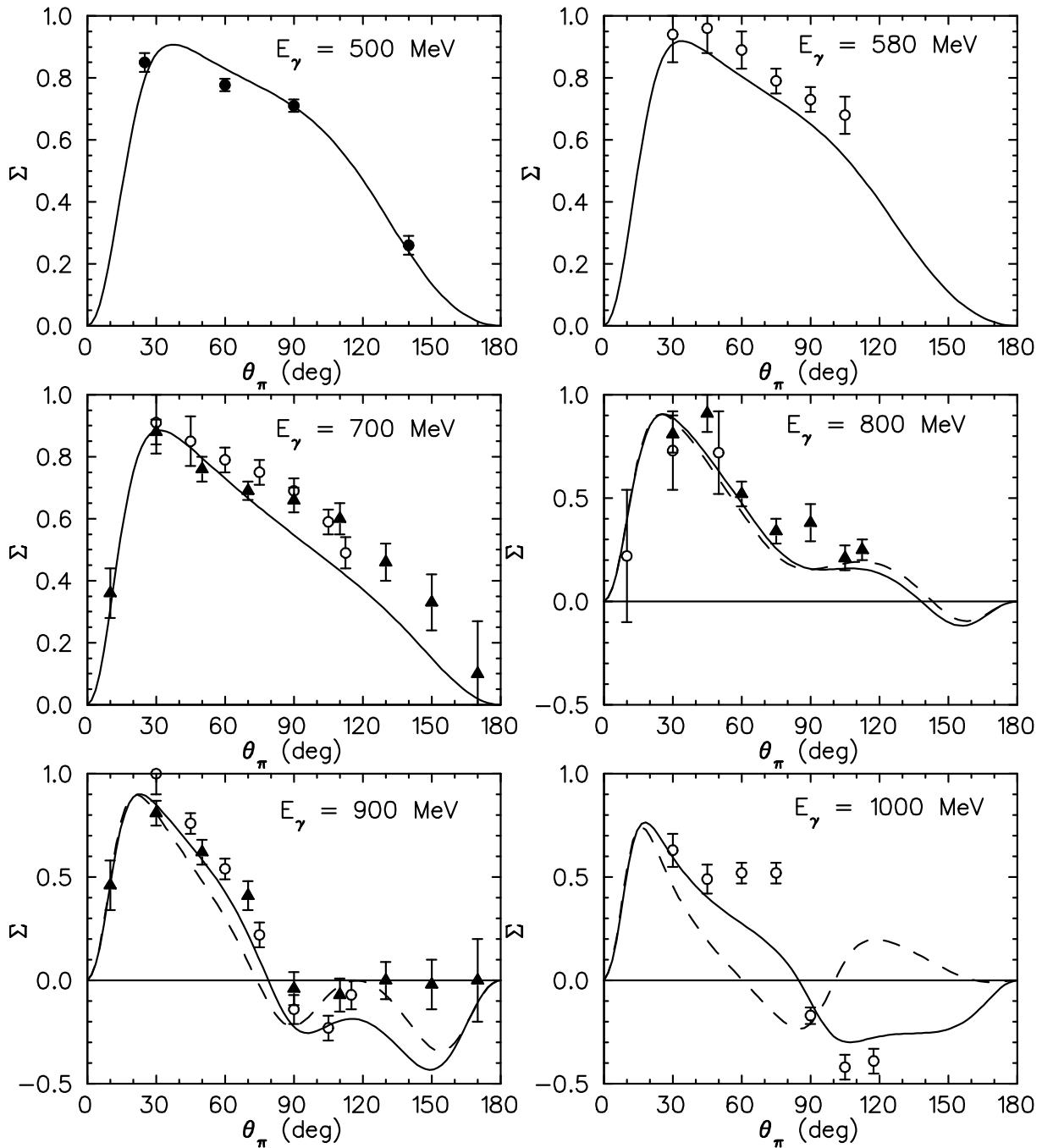


FIG. 12. Photon asymmetries  $\Sigma$  for  $p(\gamma, \pi^+)n$ . The dashed curves are the results obtained without the  $S_{11}(1650)$  resonance. Experimental data from Refs. [36–38].

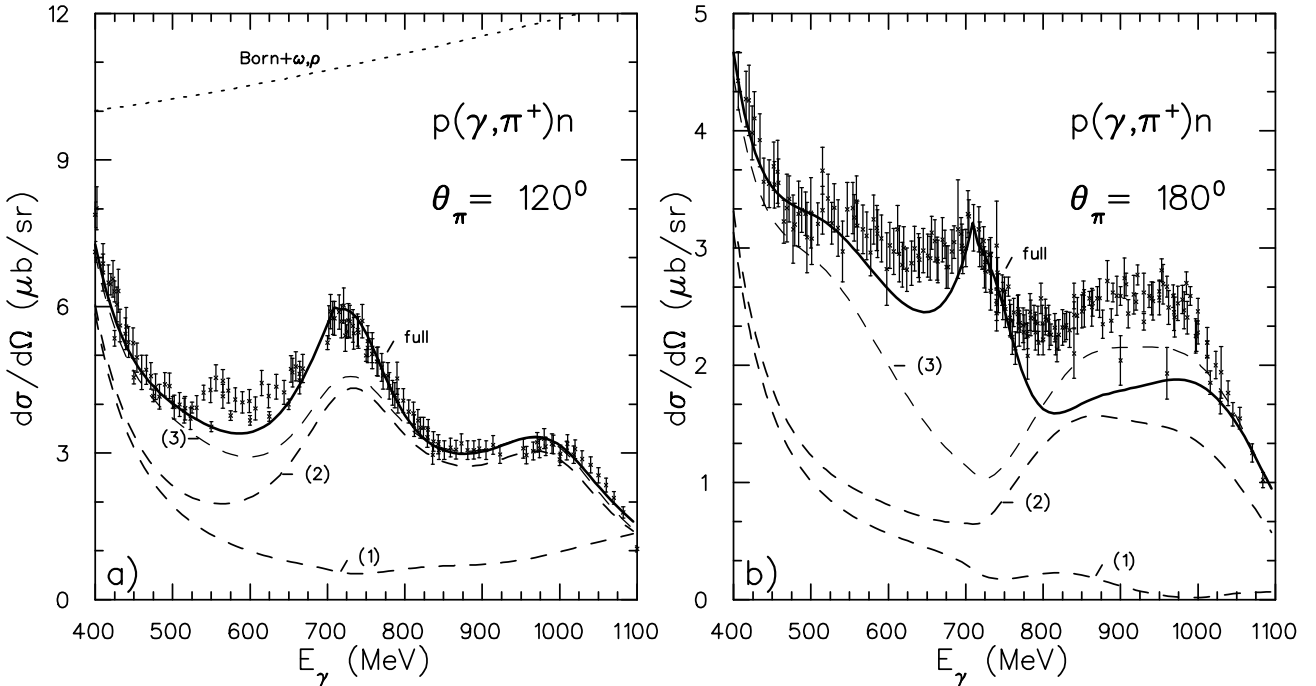


FIG. 13. Differential cross sections for  $p(\gamma, \pi^+)n$  at  $\theta_\pi = 120^\circ$  (a) and  $\theta_\pi = 180^\circ$  (b). The dotted curve is the  $Born + \omega, \rho$  contribution. The dashed curves are the results obtained with subsequent addition of the baryon resonances: (1)  $Born + \omega, \rho + P_{33}(1232)$ ; (2)=(1)+ $D_{13} + F_{15} + D_{33}$  and (3)=(2)+ $P_{11}(1440)$ . The solid curves are the full calculations which include the  $S_{11}(1535)$  resonance. Experimental data from the VPI compilation.

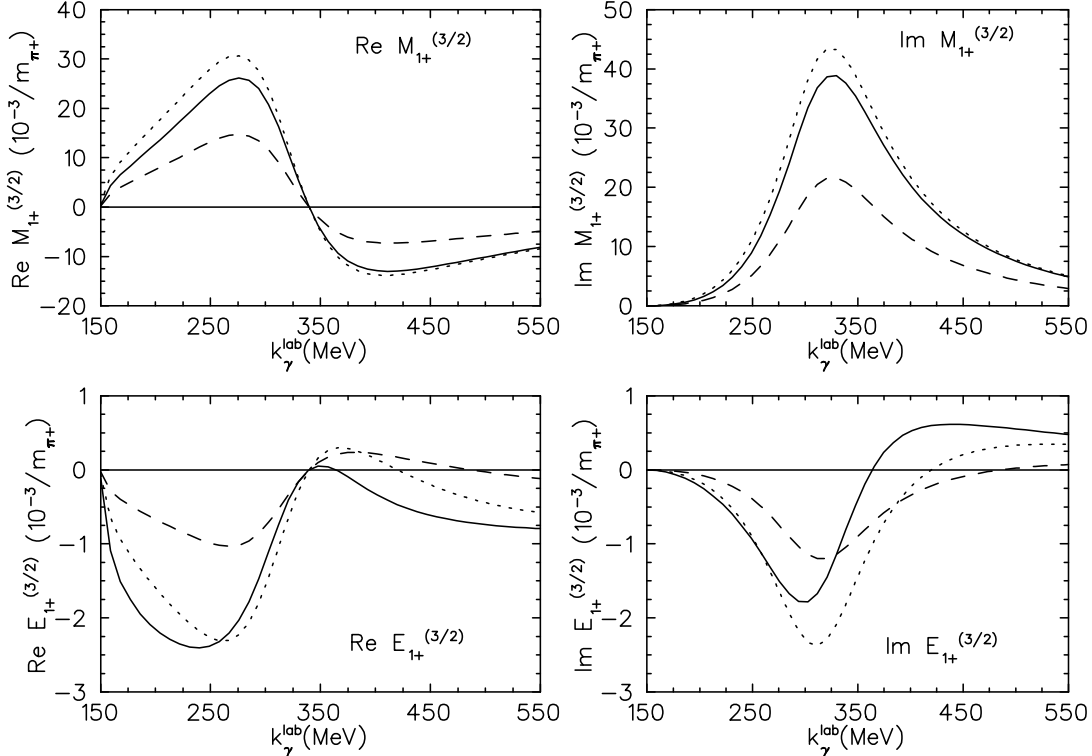


FIG. 14. The real and imaginary parts of the unitarized  $M_{1+}^{(3/2)}$  and  $E_{1+}^{(3/2)}$  multipoles at  $Q^2 = 0$  (solid curves),  $Q^2 = 0.2 (GeV/c)^2$  (dotted curves) and  $Q^2 = 1.0 (GeV/c)^2$  (dashed curves), as a function of the photon equivalent energy  $k_\gamma^{lab} = (W^2 - m_N^2)/2m_N$ .

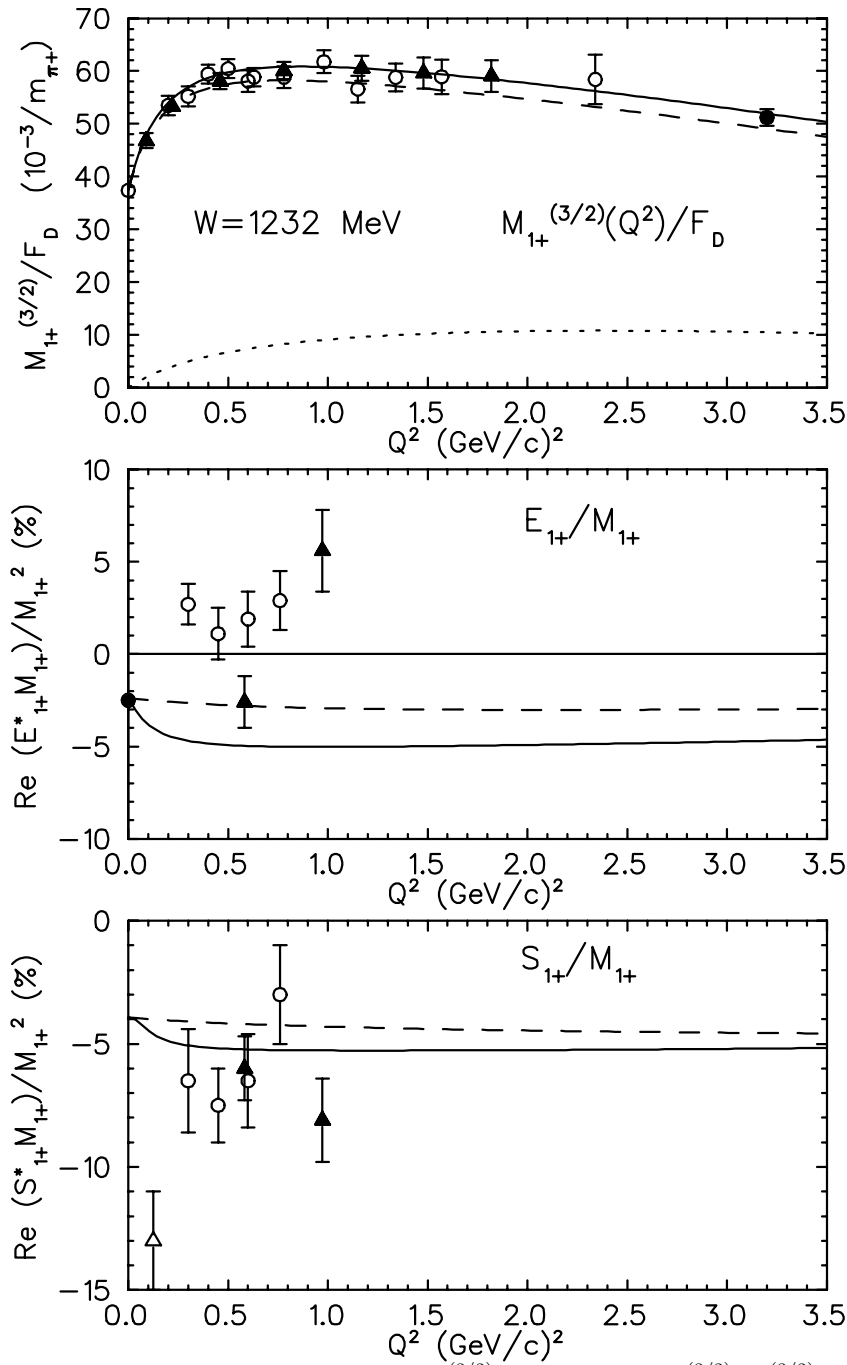


FIG. 15. The  $Q^2$  dependence of  $\text{Im } M_{1+}^{(3/2)}$  and the ratios  $E_{1+}^{(3/2)}/M_{1+}^{(3/2)}$  and  $S_{1+}^{(3/2)}/M_{1+}^{(3/2)}$  at  $W = 1232$  MeV. The full and dashed curves are the results obtained with and without unitarization respectively. In the latter case the real part of  $M_{1+}^{(3/2)}$  does not vanish at resonance as shown by the dotted curve ( $-\text{Re } M_{1+}^{(3/2)}/F_D$ ). Experimental data for  $M_{1+}^{(3/2)}$  from Refs. [39,46,47], for  $E_{1+}/M_{1+}$  and  $S_{1+}/M_{1+}$  from Refs. [48–50].

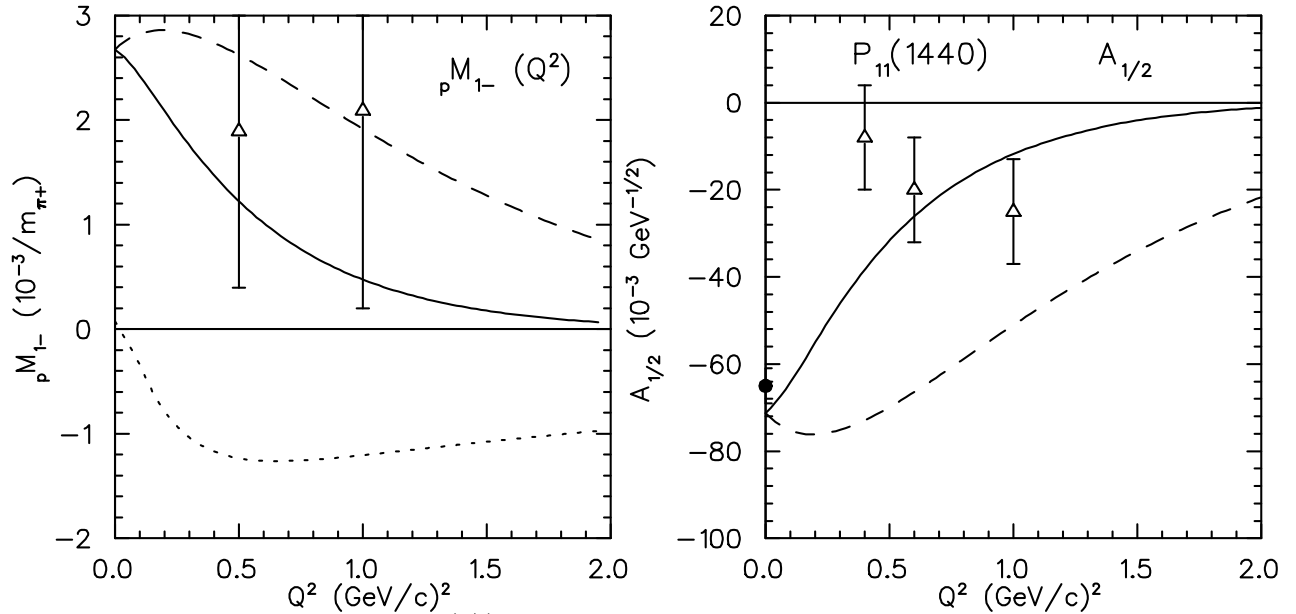


FIG. 16. The  $Q^2$  dependence of  $\text{Im } {}^p M_{1-}^{(1/2)}$  and the corresponding helicity amplitude  $A_{1/2}$ , calculated with the  $P_{11}(1440)$  resonance at  $W = 1460$  MeV. The dashed curves are the results obtained without unitarization. The dotted curve is  $\text{Re } {}^p M_{1-}^{(1/2)}$  in the non-unitarized case. Experimental data for  ${}^p M_{1-}^{(1/2)}$  multipole from Ref. [39] and for  $A_{1/2}$  from Refs. [41,42].

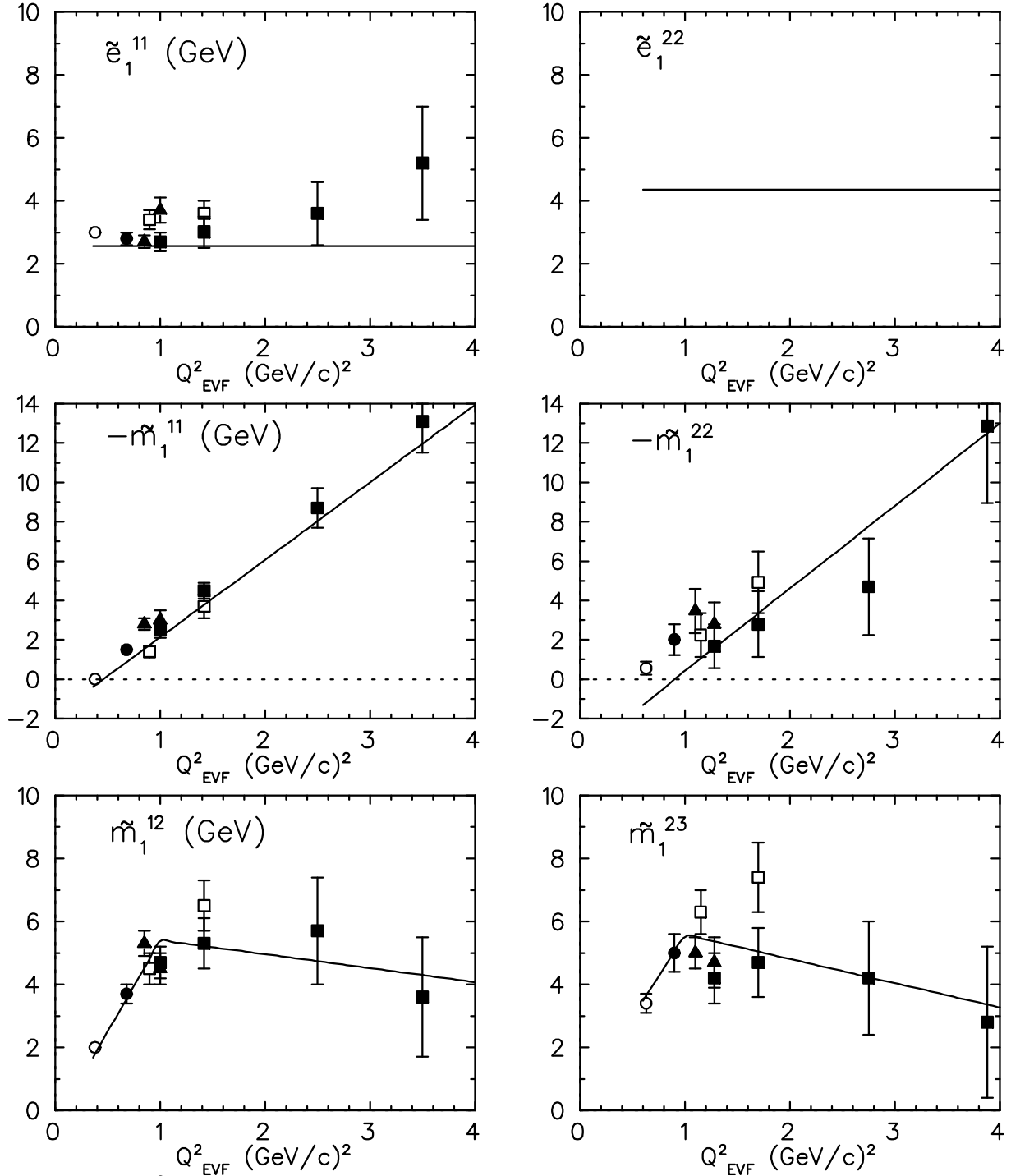


FIG. 17. The  $Q^2_{EVF}$  dependence of the reduced quark multipole moments corresponding to the parametrization (30-31). Experimental data from Ref. [41].

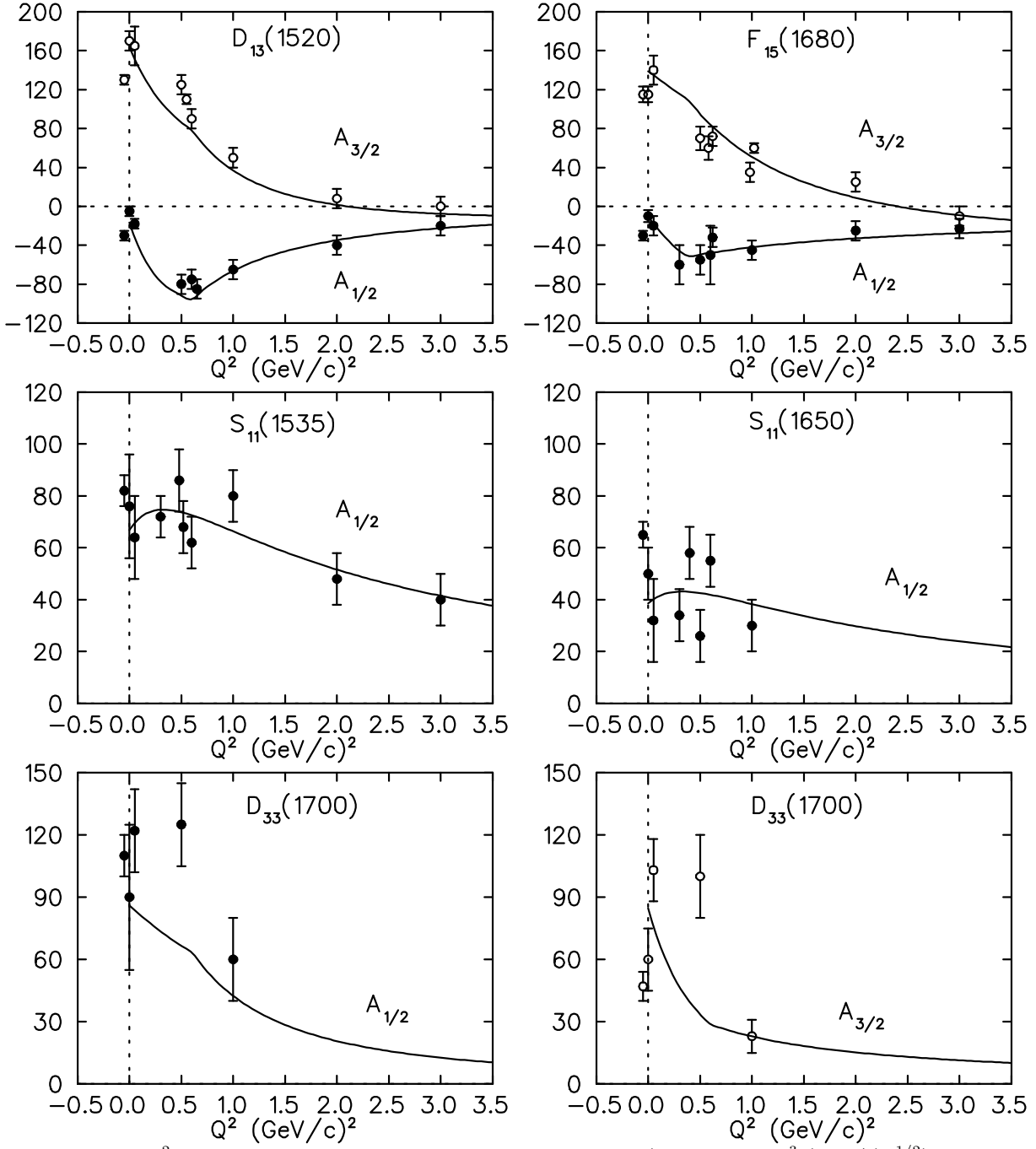


FIG. 18. The  $Q^2$  dependence of some important helicity amplitudes (in units of  $10^{-3} (\text{GeV}/c)^{-1/2}$ ) corresponding to the parametrization (30-31) for the quark multipole moments. Experimental data from Ref. [41].

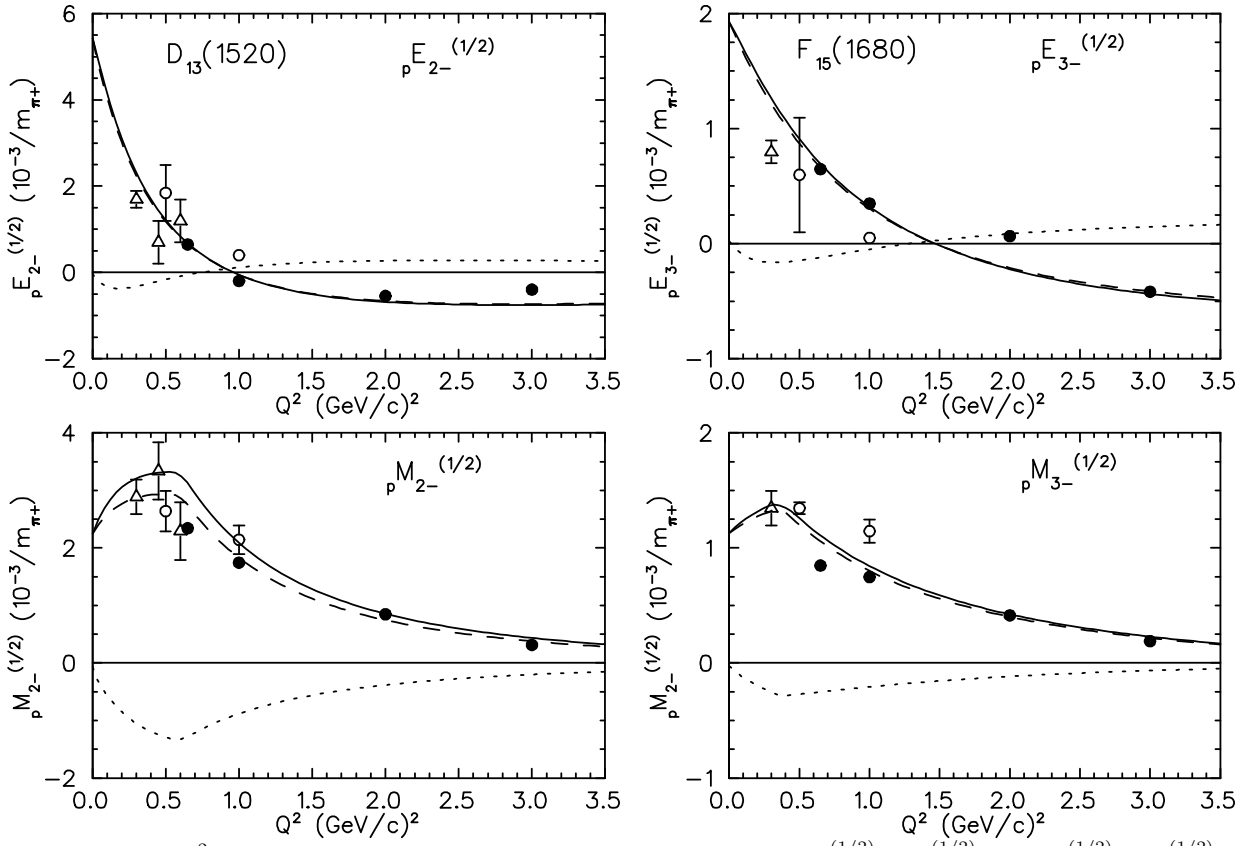


FIG. 19. The  $Q^2$  dependence of the imaginary parts of the unitarized  ${}^p E_{2-}^{(1/2)}$ ,  ${}^p M_{2-}^{(1/2)}$  and  ${}^p E_{3-}^{(1/2)}$ ,  ${}^p M_{3-}^{(1/2)}$  multipoles calculated with the  $D_{13}(1520)$  and  $F_{15}(1680)$  resonances (full curve). The dashed and dotted curves are the imaginary and real parts, respectively, in the non-unitarized case. Experimental data from Ref. [39].

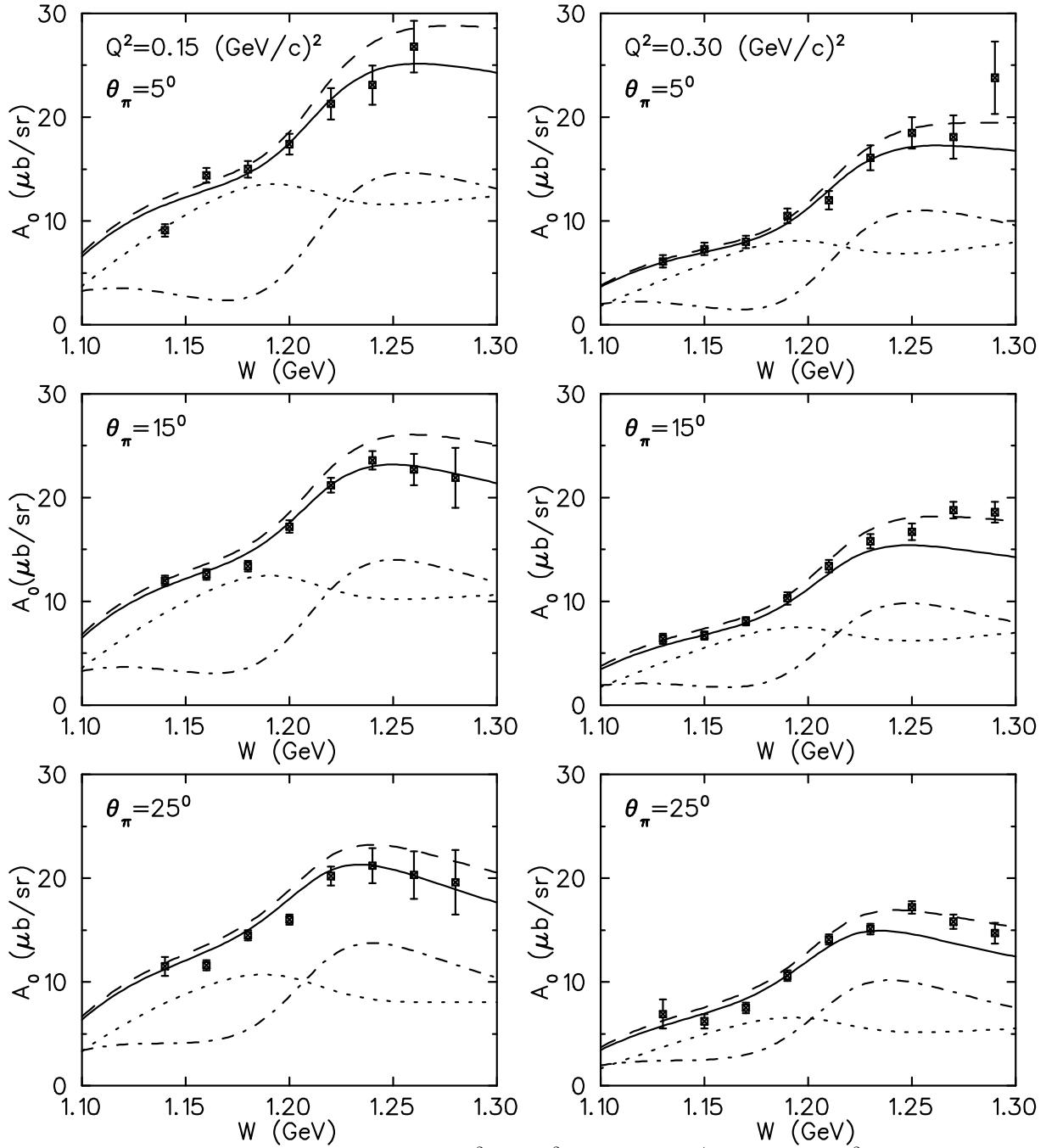


FIG. 20. The  $W$  dependence of  $A_0 = d\sigma_T/d\Omega + \epsilon Q^2 d\sigma_L/(\omega^2 d\Omega)$  for  $p(e, e'\pi^+)n$  at  $\epsilon = 0.9$ ,  $Q^2 = 0.15$  and  $0.30 \text{ (GeV/c)}^2$  and  $\theta_\pi = 5^\circ, 15^\circ, 25^\circ$ . The solid and dashed curves are the full calculations and the results without  $P_{11}(1440)$  resonance, respectively. The dotted and dash-dotted curves are the full calculations for  $Q^2 d\sigma_L / (\omega^2 d\Omega)$  and  $d\sigma_T / d\Omega$  respectively. Experimental data from Ref. [51].

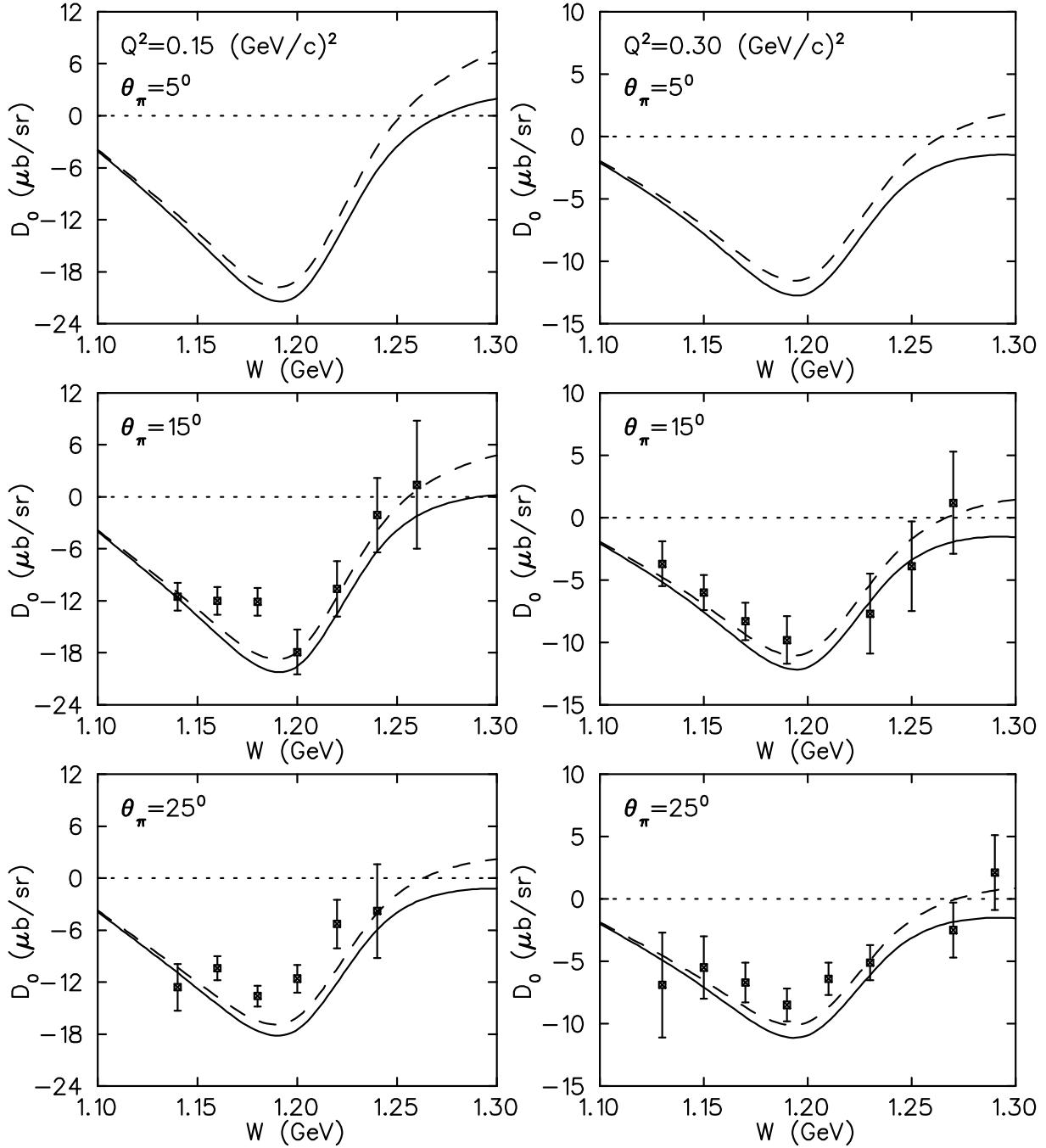


FIG. 21. The same as in Fig. 20 for  $D_0 = \sqrt{2Q^2}d\sigma_{TL}/(\omega \sin \theta_\pi d\Omega)$ . Experimental data from Ref. [51].

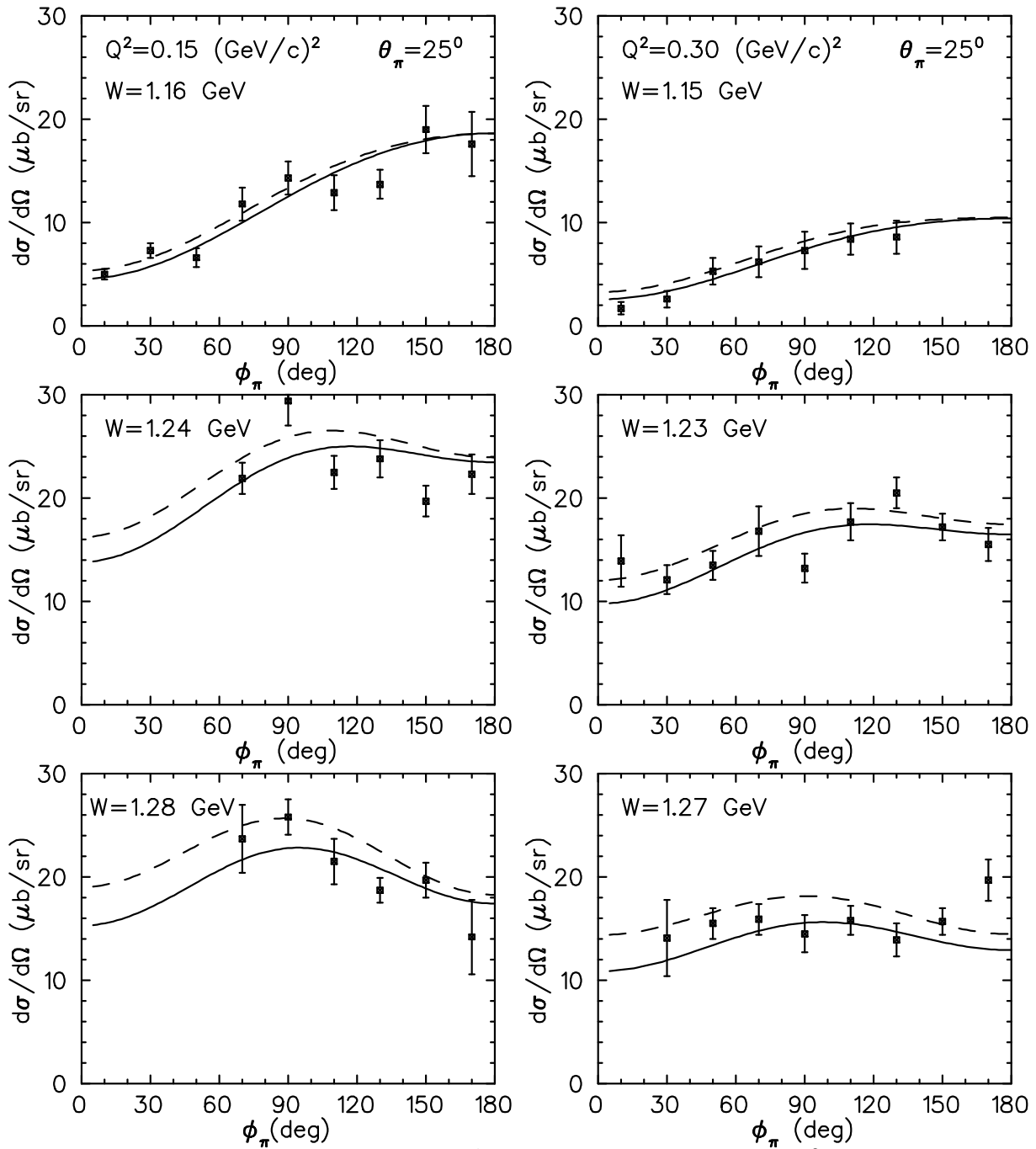


FIG. 22. The  $\phi_\pi$  dependence of  $d\sigma/d\Omega$  for  $p(e, e'\pi^+)n$  in the first resonance region at  $Q^2 = 0.15$  and  $0.30$  ( $GeV/c$ ) $^2$  and for  $\epsilon = 0.9$ . The solid and dashed curves are obtained with and without the  $P_{11}(1440)$  resonance, respectively. Experimental data from Ref. [51].

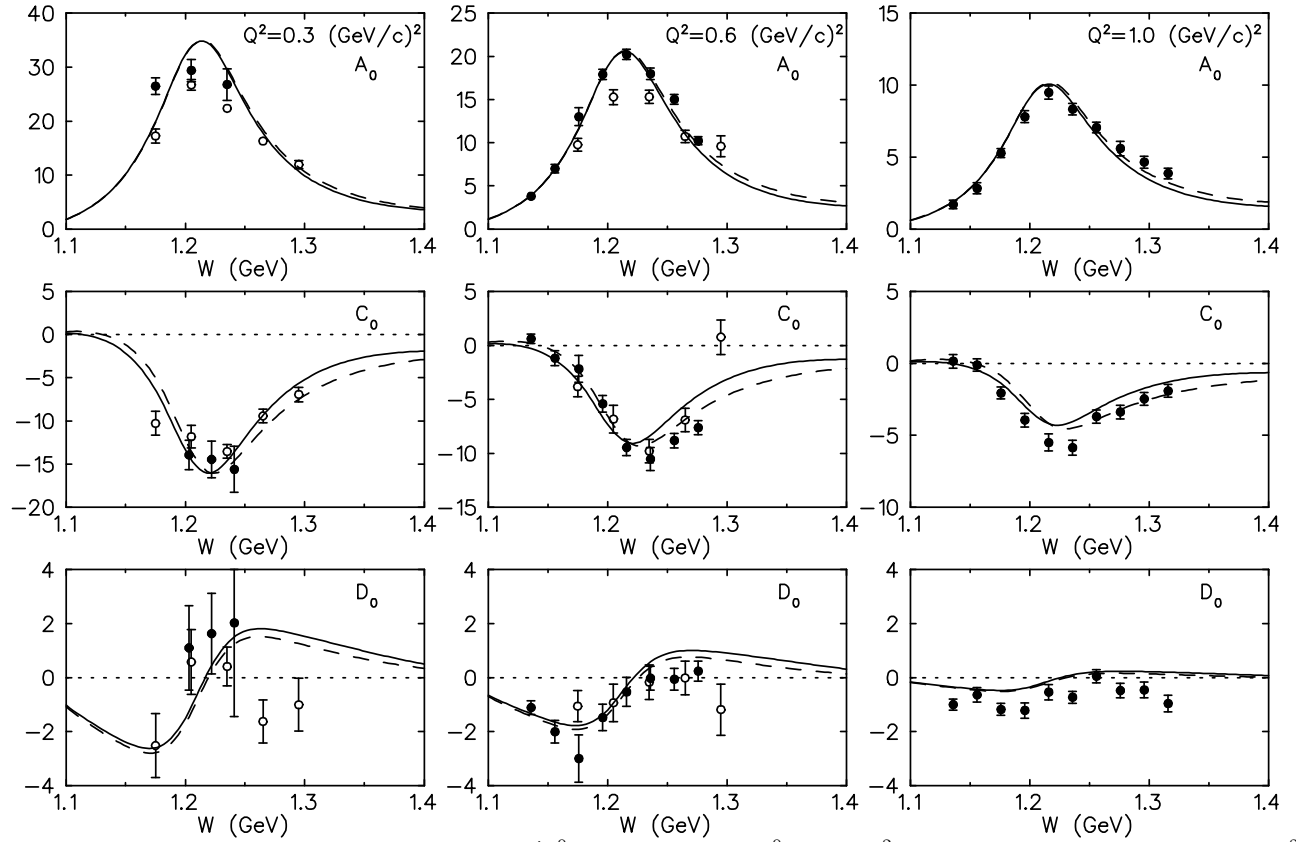


FIG. 23. The  $W$  dependence for  $p(e, e'\pi^0)p$  at  $\theta_\pi = 90^\circ$  and  $Q^2 = 0.3, 0.60$  and  $1.0 \text{ (GeV}/c)^2$  of  $A_0 = d\sigma_T/d\Omega + \epsilon Q^2 d\sigma_L/(\omega^2 d\Omega)$ ,  $C_0 = d\sigma_{TT}/(\sin^2 \theta_\pi d\Omega)$  and  $D_0 = \sqrt{2Q^2} d\sigma_{TL}/(\omega \sin \theta_\pi d\Omega)$  (in  $\mu b/\text{sr}$ ). The solid and dashed curves are obtained with and without the  $P_{11}(1440)$  resonance, respectively. Experimental data from Refs. [48,49].